Citation for final published version:

Abdpour, Soheil, Kowsari, Elaheh, Bazri, Behrouz, Moghaddam, Mohammad Reza Alavi, Tafreshi, Saeedeh Sarabadani, de Leeuw, Nora H. , Simon, Ilka, Schmolke, Laura, Dietrich, Dennis, Ramakrishna, Seeram and Janiak, Christoph 2020. Amino-functionalized MIL-101(Cr) photodegradation enhancement by sulfur-enriched copper sulfide nanoparticles: an experimental and DFT study. Journal of Molecular Liquids 319 , 114341. 10.1016/j.molliq.2020.114341

Publishers page: http://dx.doi.org/10.1016/j.molliq.2020.114341

Amino-functionalized MIL-101(Cr) photodegradation enhancement by sulfur-enriched copper sulfide nanoparticles: An experimental and DFT study

Soheil Abdpour [a], Elaheh Kowsari [a,] , Behrouz Bazri [a], Mohammad Reza Alavi Moghaddam [b], Saeedeh Sarabadani Tafreshi [a], Nora H. de Leeuw [c], Ilka Simon [d], Laura Schmolke [d], Dennis Dietrich [d], Seeram Ramakrishna [e], Christoph Janiak [d]

[a] Department of Chemistry, Amirkabir University of Technology, No. 424, Hafez Avenue, 1591634311 Tehran, Iran
[b] Department of Civil &Environmental Engineering, Amirkabir University of Technology, Hafez Avenue, Tehran 15875-4413, Tehran, Iran
[c] School of Chemistry, Cardiff University, Main Building, Park Place, Cardiff CF10 3AT, United Kingdom
[d] Institut fur Anorganische Chemie und Strukturchemie, Universität Düsseldorf, 40204 Düsseldorf, Germany
[e] Department of Mechanical Engineering, Center for Nanofibers and Nanotechnology, National University of Singapore, Singapore 119260, Singapore

article info

Keywords:
Metal-organic frameworks
Copper sulfide nanoparticles
Photocatalyst
Rhodamine B
Direct Z-scheme mechanism
Density functional theory calculations

abstract

In the present work, a direct Z-scheme composite photocatalyst, NH_2-MIL-101(Cr)@CuS, with high photodegradation efficiency of Rhodamine B (RhB) degradation in the visible light spectrum, is fabricated through a solvothermal method. It was found that the NH_2-MIL-101(Cr)@CuS composite with an appropriate amount of NH_2-MIL-101(Cr) exhibited high catalytic performance in the RhB photodegradation. The photocur-rent density and results from the electrochemical impedance spectroscopy (EIS) analysis confirm the promoted photocatalytic activity of the NH_2-MIL-101(Cr)@CuS composite compared to the pristine MIL-101(Cr) and CuS nanoparticles, which were supported by the electron lifetime (τ_n) calculations for the samples. The trapping ex-periments and Mott-Schottky analysis revealed that the superoxide radicals ($\bullet O_2^-$) played an essential role in the photodegradation of RhB and the promoted photocatalytic activity contributed to a direct Z-scheme mechanism between CuS and NH_2-MIL-101(Cr). Stability study also shows acceptable results during photocatalytic reaction. Furthermore, Density Functional Theory (DFT) calculations were performed to gain a better understanding of the electronic properties of the NH_2-MIL-101(Cr)@CuS nanocomposite. The calculated band structures showed that the nanocomposite has a higher photocatalytic efficiency in the visible region compared to the pristine MIL-101 (Cr) and CuS. The calculated band gap of both the semiconductors and the hybrid nanocomposite confirms the experimental results.

1. Introduction

The increase in urban and industrial activities of our societies has led to growing amounts of pollutants being released into the environment, which causes severe problems for water quality. The presence of organic dyes in water resources, used for example, in industrial processes for textiles, food, leather, paint or coatings, leads to many problems such as non-aesthetic, eutrophication, and they also endanger human health [1,2]. There are several traditional techniques for the remediation of dye molecules in wastewater, including physical and biological technologies that are, however, incapable of achieving efficient degradation of the dye molecules [3–8]. In recent years, interest has grown into the use of solar energy and semiconductor photocatalysis in water purification, e.g., the pollutants degradation process, the photocatalytic green fuel production, and the conversion of greenhouse molecules into fuels or chemicals [9–12]. Also, the specific functionalization of compounds for specific roles in their environment and targeting using green surfactants has a bright future [13,14]. Several photocatalytic materials, including metal oxides, metal sulfides, metal phosphides, and metal-organic frameworks (MOFs), have been studied for water purification through the photodegradation of pollutants molecules [15–19]. Some innovative findings include in the study on the composite products with enhanced morphology as well as the improved Z-scheme- charge-carriers separa-tion and plasmon-induced injection for the photocatalytic process [20,21], increasing the utilization efficiency of visible light by doping [22], and the new combination of the process like the interaction be-tween photocatalysts and microorganisms [23].

Copper (II) sulfide (CuS) is one of the most promising semiconduc-tor materials with excellent optical, electronic, chemical, and thermal

---

Corresponding author.

E-mail address: kowsarie@aut.ac.ir (E. Kowsari).

properties [24–31]. It is a p-type semiconductor with a broad reported range for its bandgap (1.63–2.56 eV) [32,33]. CuS has attracted much at-tention as a co-catalyst to improve the photocatalytic performance of a wide range of materials, e.g., in combination with metal oxides and metal sulfides, as well as carbonaceous graphitic carbon nitride (g-CN), and also for the fabrication of efficient hybrid/composite materials with carbon-based materials like graphene oxide for energy conversion applications [34–37].

Metal-organic frameworks define as hybrid inorganic/organic crys-talline materials designed as metal clusters and organic linkers, which have the potential application of impurity removal in aqueous solutions [38–41]. Flexibility in the linker design of MOFs, their high surface area and porosity have led to the use of MOFs in various scientific and tech-nological fields, including gas storage, gas separation, drug delivery, sensors, supercapacitors, heat transfer, water adsorption, catalytic and photocatalytic applications [8,42–44]. Alvaro et al. [45] first proposed MOF-5 as a catalyst for the photodegradation of water contaminants, and after that, many types of research studies have focused on MOFs as photoactive materials for energy applications [45–48]. However, pure MOFs have drawbacks as photocatalysts, corresponding to a high electron-hole recombination rate and partial adsorption of UV–visible irradiation [49–51]. Different groups of materials, including conven-tional semiconductor materials (TiO_2, ZnO, CdS, ZnS), carbon-based ma-terials (graphene oxide, g-CN), and even diverse types of MOFs have been used to fabricate active hybrid/composite photocatalysts with en-hanced photocatalytic performance compared to pure MOFs and other parent materials [52–55]. Among these diverse strategies for developing efficient hybrid/composite photocatalysts, semiconductor@MOF photocatalysts have shown considerable advantages, resulting from the synergistic effect between MOFs and conventional semiconductors [56]. Many semiconductor nanoparticles have been used for developing semiconductor@MOF systems to date, including CdS@MIL-101(Cr), ZnO@ZIF-8, TiO_2@UiO-66, ZnO@MOF-5, CdS@MIL-53(Fe), CdS@MIL-100(Fe), and Bi_2S_3@MIL-100(Fe) [56–60]. Recently, the main focus of researchers for developing new semiconductor@MOF photocatalysts is to identify new combinations of MOFs and semiconductor materials that use a direct Z-scheme charge separation mechanism, which, com-pared to traditional type-II band-to-band charge separation, shows higher redox capacity and more efficient charge carrier separation [61,62].

The primary purpose of this study was to explore the use of copper sulfide nanoparticles to enhance the photocatalytic efficiency of MOFs. The novel direct Z-scheme NH_2-MIL-101(Cr)@CuS composite with dif-ferent weight percentages of copper sulfide was developed for the oper-ative photodegradation of RhB in the visible light irradiation. The high surface area amino-functionalized MIL-101(Cr) with water-stable structure was used as a matrix to disperse the nanoparticles of copper sulfide, reduce their agglomeration, and also reduce the electron-hole recombination rate in the resulting composite structures compared to the parent materials [63]. In the photocatalytic degradation of RhB, elec-trochemical and photoelectrochemical experiments showed the excel-lent photocatalytic activity of the composite, owing to the effective interactions with NH_2-MIL-101(Cr) and copper sulfide nanoparticles, which may introduce these nanoparticles as a cost-effective, innocuous and operative co-catalyst for the development of photocatalytic com-posite systems based on MOFs.

2. Material and methods

2.1. Materials

All the chemicals (AR grade) were used without any further purifica-tion. $Cu(NO_3)_2.6H_2O$ (98%), thioacetamide (98%), $Cr(NO_3)_3{\cdot}9H_2O$ (99%) were purchased from Sigma Aldrich. Ethylene glycol (98%), NaOH (98%), and 2-Aminoterephthalic acid (99%) were purchased from Merck Company. Nafion solution (5%) was purchased from Alfa Aesar Company.

2.2. Synthesis of CuS nanoparticles

The CuS nanoparticles are synthesized via the hydrothermal ap-proach [64]. For this purpose, about 0.1215 g (0.41 mmol) of $Cu(NO_3)_2.6H_2O$ and 0.0765 g (1 mmol) of thioacetamide (TAA) stirred for 30 min to dissolve in 10 mL of ethylene glycol at ambient temperature. The mixture was then transferred into a 20 mL Teflon-lined container within stainless-steel autoclave cover and heated at 150 °C for 24 h. After cooling in ambient air, the obtained nanoparticles were separated by centrifugation at 10000 rpm for 10 min. The precipitate was washed three times with DI water and ethanol. The powder dried in a vacuum oven at 60 °C overnight. The final weight of the obtained CuS after wash-ing and drying was 0.0257 g (yield 34%.).

2.3. Synthesis of NH_2-MIL-101(Cr)

The NH_2-MIL-101(Cr) nanoparticles were also synthesized via a hydrothermal method. Typically, 3.20 g (14.7 mmol) of $Cr(NO_3)_3{\cdot}9H_2O$ and 1.44 g (8 mmol) of 2-Aminoterephthalic acid was added gradually into 60 mL of a solution of NaOH (0.33 M). The mixture was stirred at ambient temperature for 30 min and then transferred into a 100 mL Teflon-coated stainless-steel autoclave and kept at 150 °C for 12 h. Af-terwards, the cooled mixture was centrifuged at 10000 rpm for 15 min to collect the precipitate. The separated powder had green color easily visible to the naked eye. The product washed sufficient times with water, DMF, and methanol, individually, and dried overnight at 100 °C. The final weight of the NH_2-MIL-101(Cr) was 2.0 g (yield: 72%).

2.4. Synthesis of NH_2-MIL-101(Cr)@CuS composite photocatalyst

In order to synthesize the NH_2-MIL-101(Cr)@CuS composite, diverse quantities of NH_2-MIL-101(Cr) (0.05, 0.1, 0.15, 0.2, and 0.25 g) were dis-persed into ethylene glycol using ultrasound for 30 min. Then 0.1215 g (0.41 mmol) of $Cu(NO_3)_2{\cdot}6H_2O$ was added to the suspension and mixed for 30 min. After the complete dissolution of $Cu(NO_3)_2{\cdot}6H_2O$, 0.0756 g (1 mmol) of TAA added to the suspension and stirred for an-other 30 min. The resulting mixture was transferred to a Teflon-lined stainless-steel autoclave and heated at 150 °C for 24 h. The samples are called after the initial weight of NH_2-MIL-101(Cr) nanoparticles as 0.05-NM@CuS, 0.1-NM@CuS, 0.15-NM@CuS, 0.20-NM@CuS, and 0.25-NM@CuS for the products with 0.05, 0.1, 0.15, 0.2, 0.25 g of NH_2-MIL-101(Cr), respectively.

2.5. Characterization

The powder diffraction x-ray analysis (PXRD) measurement of the samples was carried out at room temperature in a BRUKER D2 Phaser in 2θ angles with Cu Kα radiation (λ = 1.54182 Å) at a voltage of 35 kV. The FT-IR spectra of the samples were recorded on a Bruker Ten-sor 37 IR spectrometer (Bruker Optics, Ettlingen, Germany) with the ATR unit. Scanning electron microscopy (SEM) was performed with a Jeol JSM-6510LV QSEM Advanced microscope with tungsten (Wolfram, W) cathode (5–20 keV). The Bruker Xflash 410 silicon drift detector was used in the microscope, and Bruker ESPRIT software applied for energy-dispersive X-ray spectroscopic (EDX) analysis. Transmission electron microscopy (TEM) images were taken on deposited samples on 200 μm carbon-coated gold grids using a FEI Tecnai G20, operating at an accelerating voltage of 200 kV. Selected-area electron diffraction (SAED) patterns were recorded with a FEI Tecnai G2 F20. Averaged dif-fraction patterns of 3 measurements were recorded and described. HR-XPS (ESCA) measurements were conducted on a Fisons/VG Scientific ESCALAB 200× xp spectrometer, functioning at 80 °C, a pressure of

1.0×10^{-9} bar, and a sampling angle of 33°. Polychromatic Al Kα exci-tation (11 kV, 20 mA) was used for recording spectra (emission angle: 0°, reference: carbon 1 s orbital with a binding energy of 284.8 eV). A Micrometrics ASAP 2020 automatic gas sorption analyzer, armed with oil-free vacuum pumps (ultimate vacuum $<10^{-8}$ mbar), was used to measure the sorption isotherms. The samples were attached to the preparation port of the device and were degassed under high vacuum for 6 h at 120 °C. Nitrogen sorption isotherms were measured at 77 K (liquid nitrogen cooling). UV–Visible measurements were carried out with a UV–Vis SPECORD S600 (2012) from Analytik Jena, a simulta-neous measuring spectrophotometer with polychromator construction and measuring the range of 190–1100 nm. The photoluminescence analysis was done by a PerkinElmer (USA) (model LS50B). The chromium leached after the photocatalytic reaction was determined by ICP-OES (730-ES, VARIAN). All electrochemical and photoelectrochemical experiments were carried out by IVIUM potentiostat/galvanostat (VERTEX entry-level instrument).

2.6. Photocatalytic tests

The photocatalytic performance of the samples was determined by photodegradation of RhB under visible light irradiation (500 W xenon lamp, with a 420 nm UV-cutoff filter) in the open air at controlled room temperature. The xenon lamp was kept at a fixed distance to the photocatalytic reactor in order to provide the standard condition (100 mW/cm^2) during photocatalytic tests. In a typical experiment, 10 mg of photocatalyst sample was dispersed into 100 mL of RhB aque-ous solution (10 mg/L) in a 200 mL cylindrical Pyrex vessel reactor with a quartz window. The pH of the as-prepared suspension adjusted to 7.0. The suspension was sonicated for 15 min and then stirred magnetically in the dark condition for 2 h to reach the adsorption/desorption equilib-rium. During the photocatalytic degradation reaction, 3 mL of the sus-pension was aliquoted every 10 min and centrifuged at 6000 rpm to separate the photocatalysts from the supernatant for analysis [65]. The concentration of RhB was calculated at the 552 nm absorption wavelength.

2.7. Electrochemical and photoelectrochemical measurements

A standard three-electrode configuration electrochemical cell with Ag/AgCl (sat. KCl) as a reference, Pt foil as a counter, and photocatalyst product coated on FTO substrate as a working electrode, were used for the electrochemical studies. 10 mg of the photocatalyst in 1 mL ethanol containing 30 μL Nafion solution 5 w/w% used to fabricate the working electrodes. The resulting suspension was irradiated with ultrasound for 30 min, and after that, 10 μL of the suspension was drop-coated on the FTO substrate and dried overnight in a vacuum oven at 50 °C. The electrochemical impedance spectroscopy (EIS) (open circuit potential: 10^5 and 10^{-2} Hz), Mott-Schottky, and chronoamperometry tests were carried out using IVIUM potentiostat/galvanostat (VERTEX entry-level instrument), at 1000 Hz frequency in −1.5 V to 1 V potential range. The photocurrent density of the as-prepared samples was measured at the set potential of 0.35 V during 220 s with 10 s dark and light cut-off. All of the electrochemical measurements were performed under similar conditions in a 0.5 mol/L Na_2SO_4 solution as the electrolyte.

2.8. Density functional theory (DFT) methodology

To have a better understanding of the interface between CuS nano-particles and NH_2-MIL-110(Cr), the electronic properties of CuS nano-particles and NH_2-MIL-110-Cr and their nanocomposite were systematically calculated using density functional theory (DFT) [66,67]. The Vienna ab initio simulation package (VASP) [68,69] with the generalized gradient approximation of Perdew, Burke, and Ernzerhof (PBE) [70] were performed for all calculations. The electron-ionic core interactions were described by the Projector augmented wave (PAW) potentials [71]. Since other studies show that the inclusion of the dispersive Van der Waals forces improves the en-ergy description of the system [72], we have employed the method of Grimme, DFT-D3 [73]. To compute the acceptable bandgap energy con-sistent with the experiment, the PBE0 [74] hybrid functional was employed, which is implemented in the VASP code, as the literature has already shown that this functional predicts more accurate band gaps for Metal-Organic Frameworks (MOFs) [75]. Since the most stable surface of CuS nanoparticles is the CuS(001) with Cu/S termination, which is the dominant surface observed on hexagonal-shaped CuS nanoparticles [76], we have investigated the interaction of the CuS

(1) surface with NH_2-MIL-110(Cr). Brillouin zone integrals were ap-proximated using the Monkhorst-Pack [77] scheme with the k-point density grid of 11 × 11 × 1 for the structural and density of state (DOS) calculations. A plane-wave cutoff energy of 560 eV was used. The geometry optimization was stopped when the total energy con-verged to within 10^{-5} eV, and the force on each ion was less than 0.01 eV/Å. To avoid interactions between periodic images, a vacuum space of more than 20 Å was set. The CuS(001) surface was modeled by a 4 × 4 supercell to make sure the cell is big enough to support NH_2-MIL-110(Cr) on top of the surface without interactions between periodic images. We have relaxed the NH_2-MIL-110(Cr) and the two top layers of the CuS(001) surface.

3. Result and discussion

3.1. Characterization of NM@CuS composites

The PXRD patterns of the pure NH_2-MIL-101(Cr), the composite se-ries, and pure CuS are presented in Fig. 1. The peak positions and diffrac-tion intensities of NH_2-MIL-101 match the observed patterns, as well as the simulated XRD for MIL-101(Cr), reported in the literature [63,78,79]. The PXRD patterns of the CuS nanoparticles confirm the presence of CuS in the structure of the obtained composite samples. The main peaks of CuS nanoparticles appeared at 2θ = 28°, 29°, 30°, 48°, 52°, and 58°. In the composite structures, both the NH_2-MIL-101 (Cr) and CuS PXRD patterns are superimposed, which confirms the presence of both components in the final product. All composite sam-ples show the same FT-IR spectra for functional peaks of NH_2-MIL-101 (Cr) (Fig. S1). The SEM images of the pure NH_2-MIL-101(Cr), pure CuS, and NM@CuS composite samples are shown in Fig. 2. In order to determine the ratio of Cr, Cu, and S in the samples, EDX elemental anal-ysis was carried out. The obtained data are shown in Table S1.

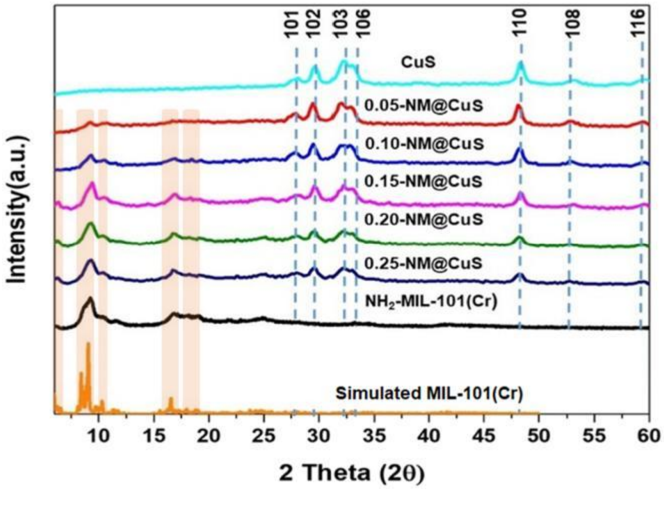

Fig. 1. PXRD patterns of the as-prepared samples of NM@CuS, NH_2-MIL-101(Cr), and pristine CuS.

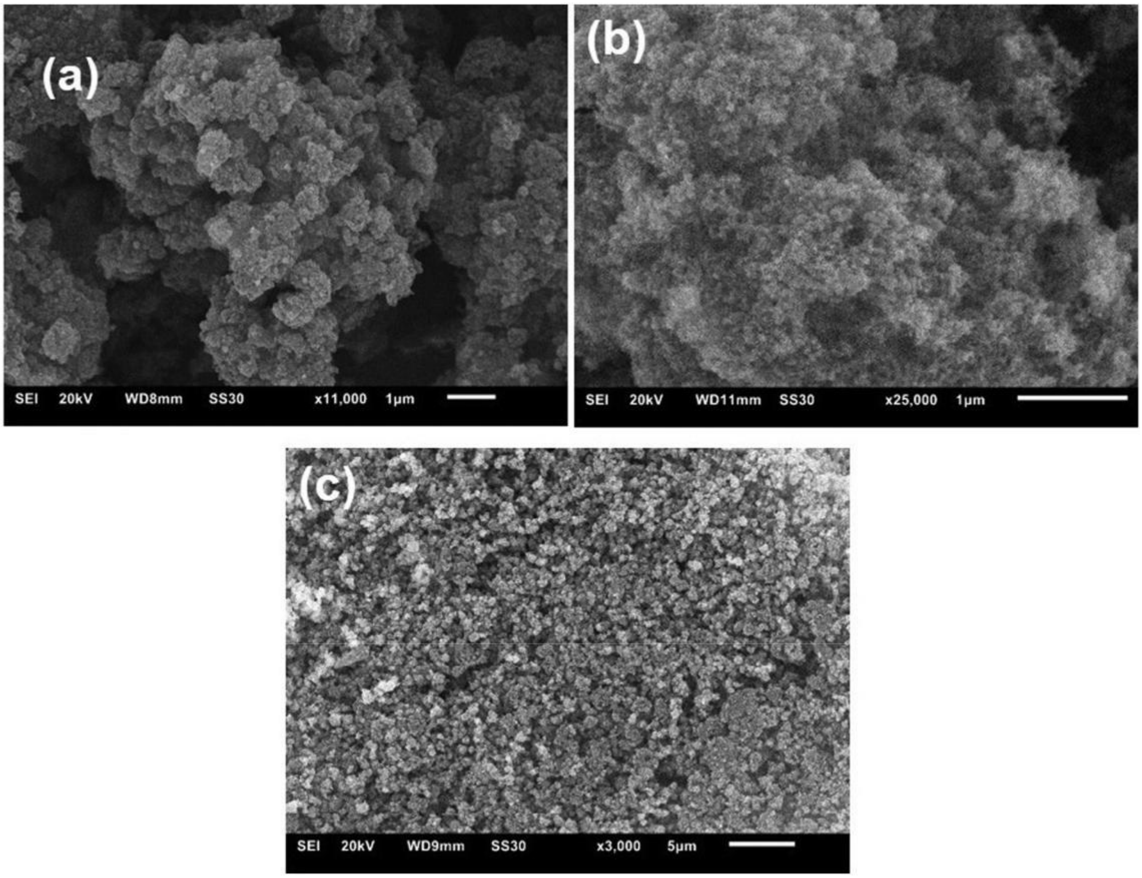

Fig. 2. SEM images of (a) NH_2-MIL-101(Cr), (b) CuS nanoparticles, (c) NM@CuS. composite.

The calculated copper and sulfur atomic ratio (Table S1) in the structures of the composites showed that by increasing the weight of the NH_2-MIL-101(Cr) in the initial suspension, the relative amount of sulfur also increased. These changes in the atomic ratio of the copper and sulfur resulted from the partial reduction of copper cations by carboxylic acid groups in the structure of NH_2-MIL-101(Cr). The same phenomenon has been detected in the presence of some other reducing agents in the reaction media [80,81].

As seen in the HR-TEM images (Fig. 3), the CuS nanoparticles, which had an average size of about 44 nm, can be distinguished from NH_2-MIL-101(Cr) (average size about 55 nm) by darker and egg-shaped morphologies.

In order to identify the phase of the CuS nanoparticles, SAED was used for four different areas on the TEM-grid, which supports the hexagonal space group of the CuS nanoparticles, whereas the diffraction rings match the literature value (hexagonal, space group P63/mmc, COD: 9008389) (Fig. 4) [82,83].

Fig. 5 presents nitrogen adsorption-desorption isotherms of the as-prepared activated NH_2-MIL-101(Cr) and composite samples, which all demonstrated the same type I isotherms due to their microporous structure [63]. By increasing the weight fraction of CuS nanoparticles in the final samples, the surface area, along with the total pore volume, was reduced. The total pore volume and surface area of the samples are exhibited in Table 1.

The XPS of the as-prepared 0.15-NM@CuS was employed to elucidate the chemical composition of the elements at the surface, considering the chemical environment of the CuS nanoparticles and NH_2-MIL-101(Cr) in the structure of the composite samples. The presence of Cu, Cr, S, N, C, and O in the as-prepared 0.15-NM@CuS was confirmed by the survey spectrum of the composite structures (Fig. 6a).

The Cr $2p_{3/2}$ orbital indicates two different Cr^{3+} species. The Cr^{3+} species at 575.6 eV can be ascribed to $Cr{-}OH_2$ and the other species at 578.0 eV can be ascribed to Cr–OH. The ratios of about 2:1 correspond to the trinuclear Cr_3 unit with two bound aqua ligands and one hydroxide ligand in NH_2-MIL-101(Cr) (Fig. 6b) [84]. The high-resolution spectrum of the Cu 2p (Fig. 6c) shows two prominent peaks at 933.3 and 953.0 eV, which can be ascribed to Cu $2p_{3/2}$ and Cu $2p_{1/2}$ in the structures of the CuS nanoparticles, whereas the small peak around 933.3 eV can be attributed to impurities of Cu^+ with the central peak at 933.5 eV ascribed to Cu^{2+}. The S 2p peak confirmed these results [85]. Furthermore, the S 2p peak (Fig. 6d) located at 163.5 eV, which splits into two peaks at 163.1 and 164.9 eV, corresponds to $S2p_{3/2}$ and $S2p_{1/2}$ which confirms the presence of sulfur metal in the structure of the NM@CuS composite materials [36,86].

The C1s, N1s, and O 1s peaks are shown in Figs. S2, S3, and S4, respectively, with the XPS analysis data shown in Table S2. All of the XPS data confirmed the presence of the NH_2-MIL-101(Cr) and CuS in the structure of the composite samples.

The optical properties of the samples were determined by diffuse reflectance spectroscopy (DRS). Fig. 7a shows the UV–Visible absorption behavior of the as-prepared samples. The adsorption band position of the NH_2-MIL-101(Cr) in the UV region was ascribed to π-π* of the ligand [87], while the low adsorption band around 600 nm can be related to the d-d spin-allowed transition of Cr^{3+} centers [56]. The UV–visible light spectrum of the composite photocatalysts, NM@CuS, indicates that the visible light absorption intensity is significantly higher than in pure NH_2-MIL-101(Cr), which can be attributed to intensive absorption of UV–Visible light by the CuS nanoparticles in the NM@CuS structures. Also, broadband extending into the near-IR region indicates the presence of CuS nanoparticles in the as-obtained composite photocatalyst materials [88].

The optical band gap energy of the samples was determined using the intercepts of the tangents of $(Ahv)^2$ vs. (hv) (Tauc plot), shown in Fig. 7b for each sample.

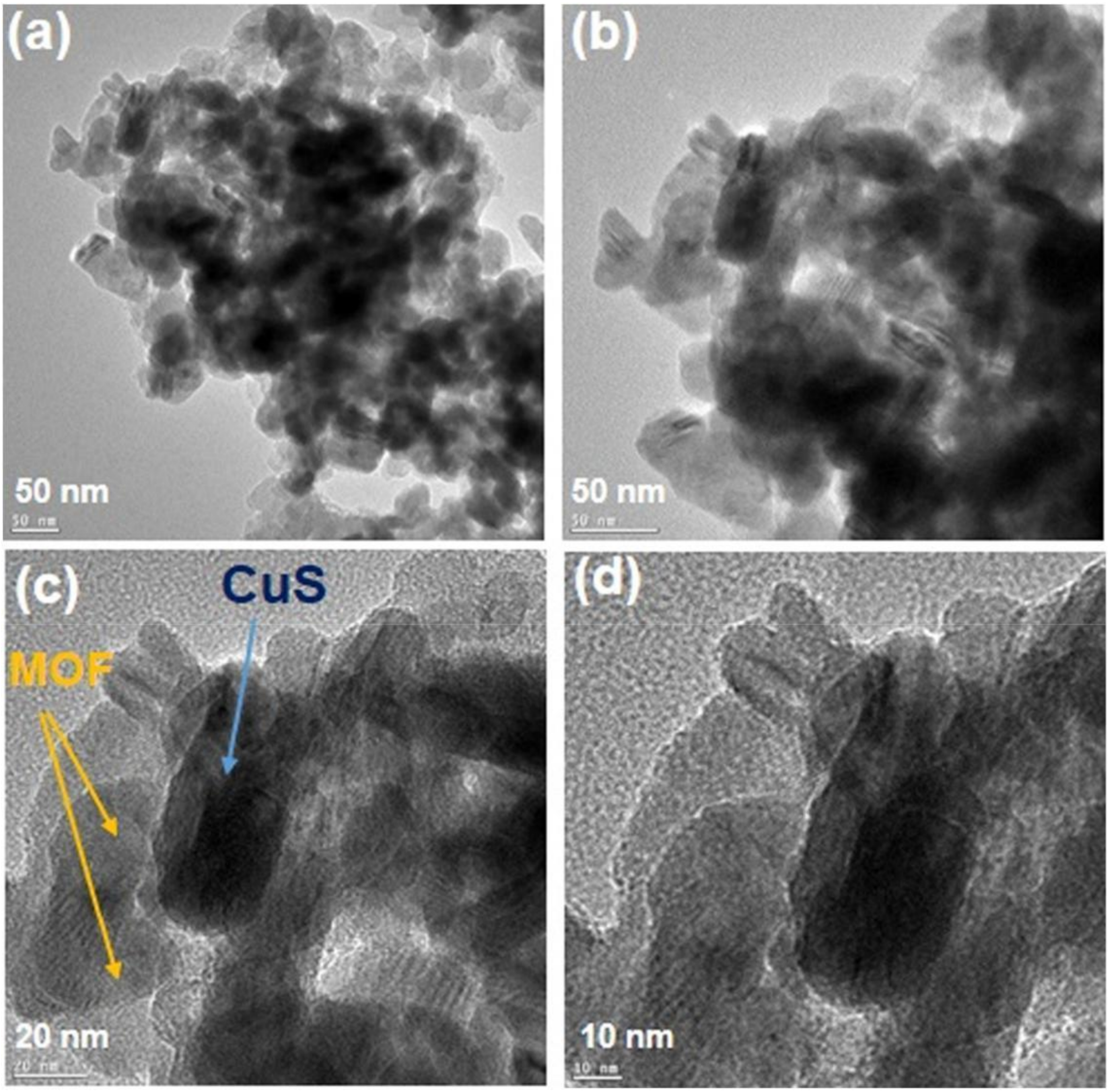

Fig. 3. (a,b,c,d) HR-TEM images of the 0.15-NM@CuS in different magnitude.

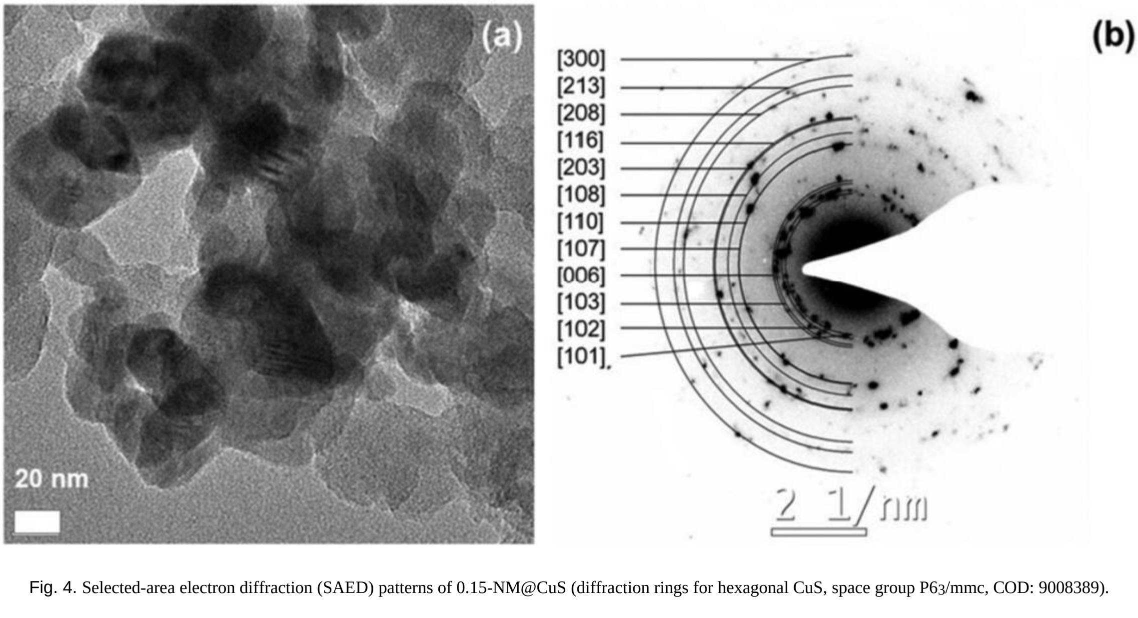

Fig. 4. Selected-area electron diffraction (SAED) patterns of 0.15-NM@CuS (diffraction rings for hexagonal CuS, space group $P6_3/mmc$, COD: 9008389).

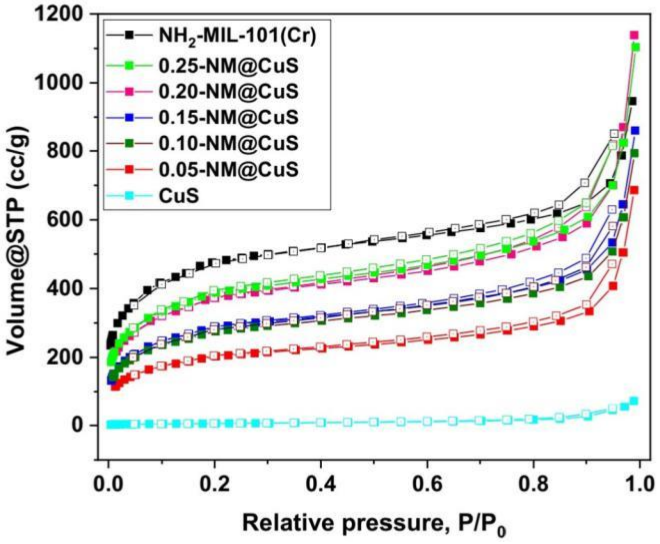

Fig. 5. Nitrogen adsorption-desorption isotherms at 77 K of the as-prepared samples. The filled and empty symbols represent adsorption and desorption, respectively.

Table 1
Surface area and pore volume values of the as-prepared samples.

Sample	BET surface area (m^2/g)[a]	Total pore volume (cm^3/g)[b]
NH$_2$-MIL-101 (Cr)	1732	0.52
0.25-NM@CuS	1411	0.38
0.2-NM@CuS	1351	0.33
0.15-NM@CuS	1041	0.27
0.1-NM@CuS	996	0.25
0.05-NM@CuS	739	0.09
CuS	21	0.01

[a] Calculated BET surface area from N$_2$ adsorption isotherms at 77 K over a pressure range of P/P$_0$ = 0.05–0.4.

[b] Total pore volume at P/P$_0$ = 0.95 for pores ≤37 nm.

α −1=2
ðhvÞ ¼ A hv Eg

where α is the absorption coefficient, v is the light frequency, E_g is the semiconductor bandgap energy, and A is the equation constant, respectively.

Thus, the band gaps of the samples were estimated from intercepts of the above equation as 1.8 (Fig. S8), 1.98, 2.05, 2.19, 2.25, 2.30, and 2.6 eV for CuS, 0.05-NM@CuS, 0.10-NM@CuS$_y$, 0.15-NM@CuS, 0.20-NM@CuS, 0.25-NM@CuS, and NH$_2$-MIL-101(Cr), respectively. The band gap values show that the optical band gap of the composite sam-ples increases with the increasing amount of the MOF in the structures of the composites.

3.2. Photocatalytic degradation of RhB

The photocatalytic performance of the as-prepared samples was evaluated via the degradation of model polluted water with RhB dye (10 ppm, pH = 7.0. room temp) under visible light irradiation (Xenon lamp 500 W). As shown in Fig. 8a, in the absence of the photocatalyst, no significant RhB degradation was observed. The concentration of RhB decreased by increasing the irradiation time, and all samples showed higher degradation performance compared to the individual parent materials.

Maximum photocatalytic degradation (C/C$_0$ = 0.06) was observed when the 0.15-NM@CuS sample was used. The photocatalytic activity of the samples was increased by increasing the number of NH$_2$-MIL-101(Cr) nanoparticles in the structure of the final composite samples, and it reached the maximum at 0.15 g of the NH$_2$-MIL-101(Cr) in the precursor suspension. Next, further increasing the NH$_2$-MIL-101(Cr) loading in the nanoparticles caused a decline in the photocatalytic per-formance, although it was still better than pure NH$_2$-MIL-101(Cr) and CuS nanoparticles. Two phenomena lead to maximum photocatalytic activity in a certain loading amount of NH$_2$-MIL-101(Cr) nanoparticles,

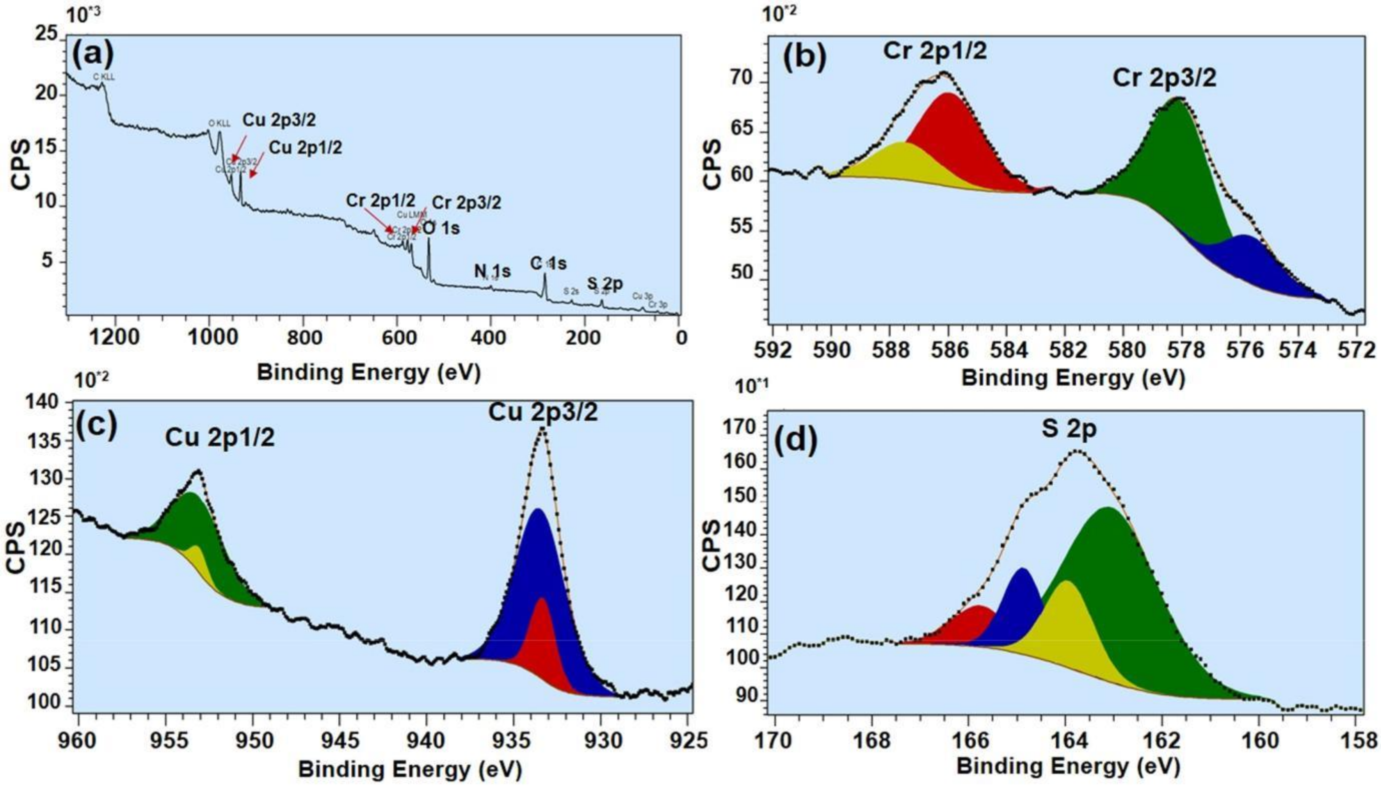

Fig. 6. XPS spectra of the 0.15-NM@CuS (a) survey spectrum, (b) Cr 2p, (c) Cu 2p, (d) S 2p region from high-resolution XPS.

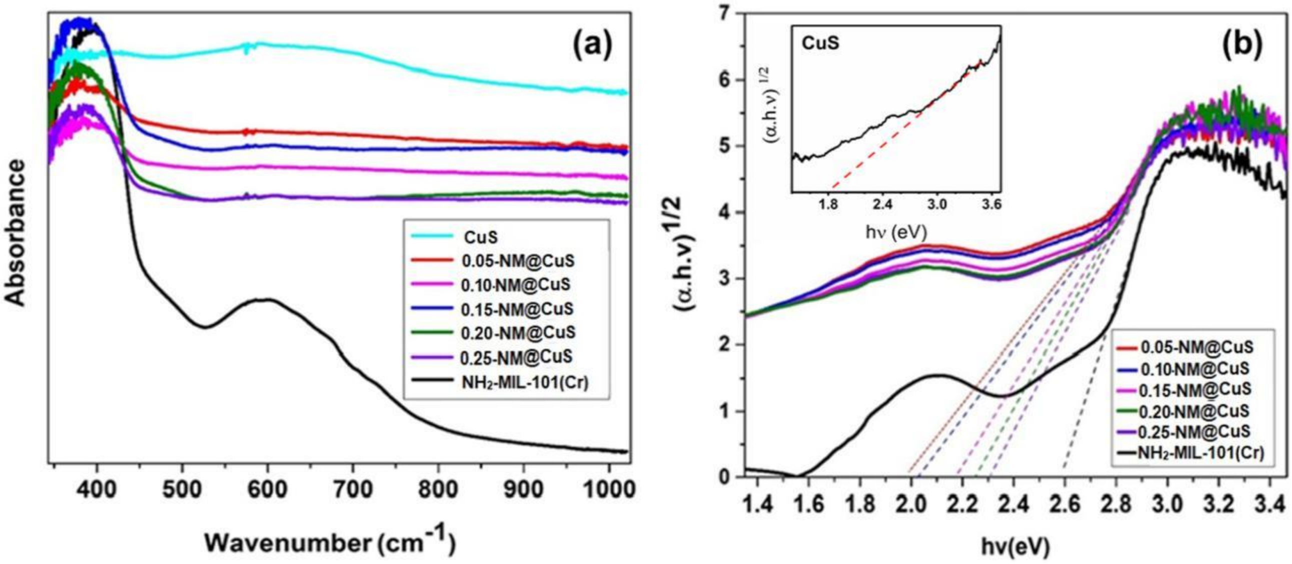

Fig. 7. (a) UV–visible absorption spectra of the as-prepared samples, (b) plot of $(\alpha h\nu)^{1/2}$ versus energy (hν) for the bandgap energy of the samples.

relating to a change in the UV–Visible light absorption and the bandgap properties of the composite samples.

The UV–visible absorption spectra of the samples (Fig. 7a) indicate that the absorption rate above 450 nm becomes more potent when the loading of NH_2-MIL-101(Cr) nanoparticles decreases, which leads to significant absorption of visible light and excitation of more electron-hole pairs. Alternatively, the bandgap of the composite sam-ples decreases with increasing loading of the copper sulfide nanoparti-cles that reduce the photocatalytic performance by increasing the electron-hole recombination rate [89].

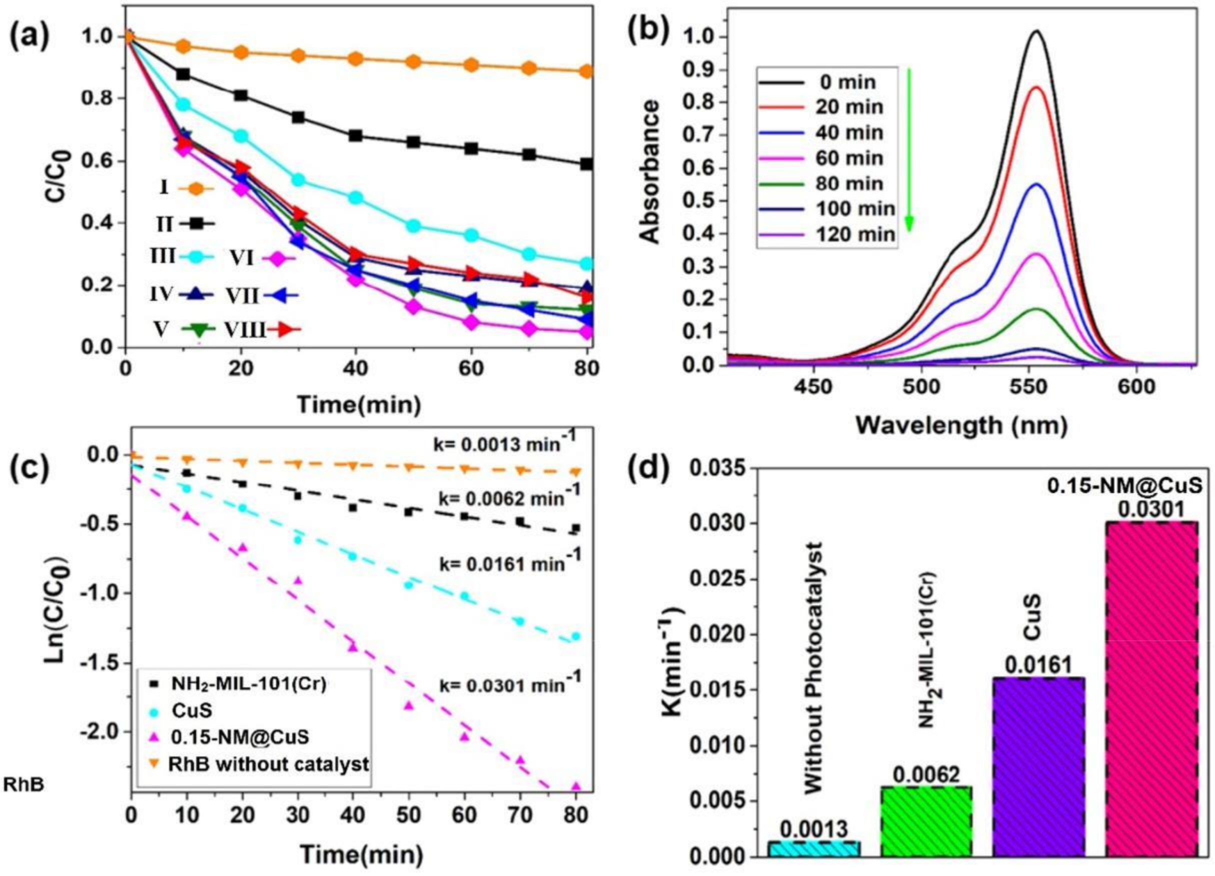

Fig. 8. (a) Photocatalytic degradation rate of RhB under visible-light irradiation (>420 nm) without and in the presence of the photocatalyst samples. (I) without catalyst, (II) NH_2-MIL-101 (Cr), (III) CuS, (IV) 0.05-NM@CuS, (V) 0.10-NM@CuS, (VII) 0.20-NM@CuS, (VI) 0.15-NM@CuS, (VIII) 0.25-NM@CuS (b) RhB absorption spectra in the presence of 0.15-NM@CuS_y in different irradiation times (c), natural logarithm C/C_0 fitting curves of NH_2-MIL-101(Cr), CuS, 0.15-NM@CuS and without photocatalyst (d), the value of the rate constant k of the photodegradation process of RhB.

Parameters such as the increase in the UV–visible absorption; de-crease in the bandgap energy levels as the amount of NH_2-MIL-101 (Cr) nanoparticles decreases; and also the effect of changing the surface area of the samples by altering the NH_2-MIL-101(Cr) loading; lead to a boost in the photocatalytic activity by loading NH_2-MIL-101(Cr) nano-particles up to 0.15 g in the composite structures. The sulfur enrichment in the NM@CuS samples can also enhance the photocatalytic perfor-mance of the samples, as is already reported for photocatalysts contain-ing copper-sulfur nanoparticles [80,90].

The change with time in the absorption spectra of RhB in the UV– visible region in the presence of 0.15-NM@CuS product is also shown in Fig. 8b. As seen in this figure, the main peak at 554 eV diminishes with time over the reaction. A kinetic study of the photocatalytic reac-tion is performed by fitting the experimental data for NH_2-MIL-101 (Cr), CuS, and 0.15-NM@CuS, by using a first-order model applying the following equation:

$$-\mathrm{Ln}(C/C_0) = kt$$

where C_0 is the RhB concentration at equilibrium after a 2-hour adsorp-tion/desorption process in dark conditions, C is the residual RhB concen-tration at time t (min) in the solution, and k is the apparent rate constant in the first-order kinetic model. As indicated in Fig. 8c,d the ap-parent constant (k) for the 0.15-NM@CuS is 1.87 times more than CuS and also 4.85 times more than NH_2-MIL-101(Cr). The higher apparent constant (k) of the 0.15-NM@CuS compared to pure NH_2-MIL-101(Cr) and CuS nanoparticles confirm the more effective photodegradation of RhB in the presence of 0.15-NM@CuS.

In Fig. 9a, the effect of raising the concentration of RhB on the photo-catalytic performance of the samples is plotted. The maximum photo-catalytic activity is observed when the initial concentration of RhB was 5 ppm (in the presence of 0.15-NM@CuS). As the RhB dye concentration increase, the photocatalytic activity reduces, which can be linked to the reduction in numbers of photons hitting the photocatalyst surfaces through extending the visible-light absorption by the dye molecules at the catalyst surfaces and in the solution [91].

The outcome of increasing the amount of photocatalyst on the photodegradation of RhB was also explored. By increasing the amount of photocatalyst (0.15-NM@CuS) from 5 mg to 40 mg, the degradation of RhB was boosted, but when the amount of photocatalyst is over 80 mg, the degradation was diminished (Fig. 9b), which could be the re-sult of shielding effects of the high concentration of photocatalyst parti-cles that inhibit the light reaching other photocatalyst particles in the suspension [92].

The stability of the photocatalyst (0.15-NM@CuS) was evaluated by 4-time cycles of the photocatalytic reaction. After each cycle, the photocatalyst was washed and dried for the next cycle. As presented in Fig. 10, after 4 cycles, about 89% of the RhB can be degraded, which shows the solidity of the photocatalyst during the cyclic photocatalytic reaction. The reduction of RhB can be attributed to a partial loss of the photocatalyst through the washing procedure of cycles of the photocat-alytic reaction. The reusability experiment and also PXRD (Fig. S5) and FT-IR spectra (Fig. S6) of the photocatalyst sample after the cyclic exper-iment prove the stability of the as-prepared composite sample during the photocatalytic reaction. The ICP-mass spectroscopy (Table S3) was also used to determine the concentration of probable leached Cr^{3+} in the solution resulting from the MH_2-MIL-101(Cr). The ICP-mass data re-vealed that no significant Cr^{3+} existed in solution, which confirms the stability of the MOF structure in the aqueous solution as the catalytic re-action proceeds.

3.3. Photocatalytic degradation mechanism of RhB over NM@CuS

In the photocatalytic degradation process of organic impurities in water, three active species play an essential role, including superoxide radicals ($\bullet O_2^-$), holes (h^+), and hydroxyl radicals (•OH), which depend-ing on the type of photocatalytic reaction, play different roles in the overall photocatalytic reaction. To determine the main active compo-nents in the photocatalytic degradation process of RhB, a trapping ex-periment was conducted (Fig. 11). Three different scavengers, benzoquinone (BQ, 0.05 mM), ammonium oxalate (AO, 0.05 mM), and tert-butyl alcohol (TBA, 0.05 mM), were used as an anion radical ($\bullet O_2^-$) scavenger, hole (h+) scavenger, and photogenerated hydroxyl radical (•OH) scavenger, respectively [93].

As shown in Fig. 11a, the photodegradation of RhB dramatically de-creased over an 80 min reaction time (C/C_0 = 55) in the presence of BQ compared to the absence of scavenger (C/C_0 = 0.06). This shows that the superoxide radicals ($\bullet O_2^-$) formed through the direct reaction of photogenerated electrons with the adsorbed oxygen molecules on the surface of the photocatalyst play an essential role in the photodegradation of RhB in the presence of NM@CuS. Also, adding a hole (h+) and hydroxyl radical (•OH) scavenger decreased the photo-catalytic degradation of RhB to about (C/C_0 = 0.27) and (C/C_0 = 0.19), respectively. The obtained data from trapping experiments re-vealed that scavengers for the superoxide radical ($\bullet O_2^-$), the hydroxyl radical (•OH), and holes (h^+) affect the photodegradation process in the presence of NM@CuS, but the superoxide radical ($\bullet O_2^-$) plays a sub-stantial role in the photocatalytic response. In contrast, the hydroxyl radical (•OH) has a less critical role. As such, the photocatalytic

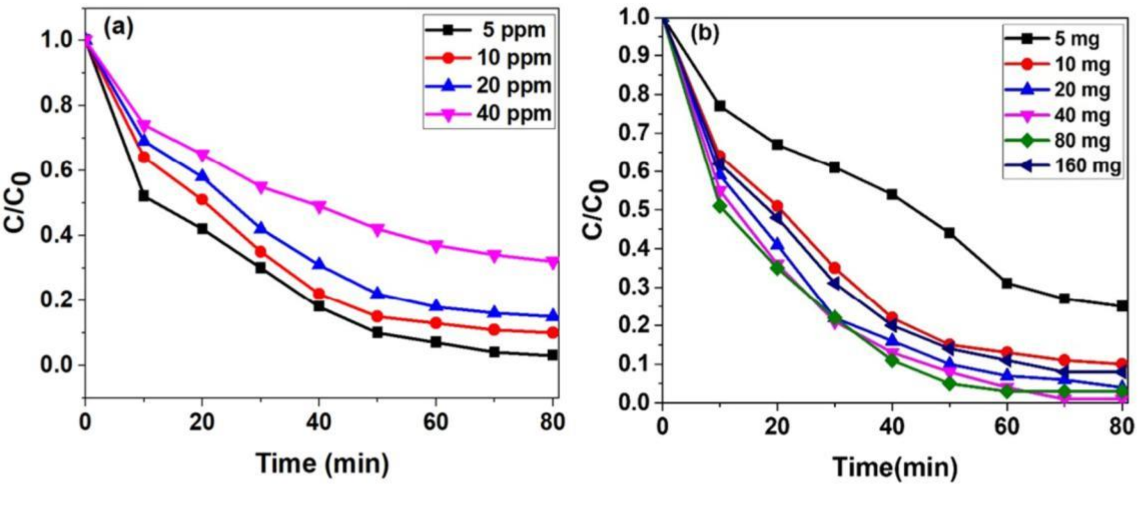

Fig. 9. (a) Effect of different RhB concentrations on the photocatalytic performance of 0.15-NM@ CuS, (b) effect of photocatalyst dosage on photocatalytic degradation of RhB.

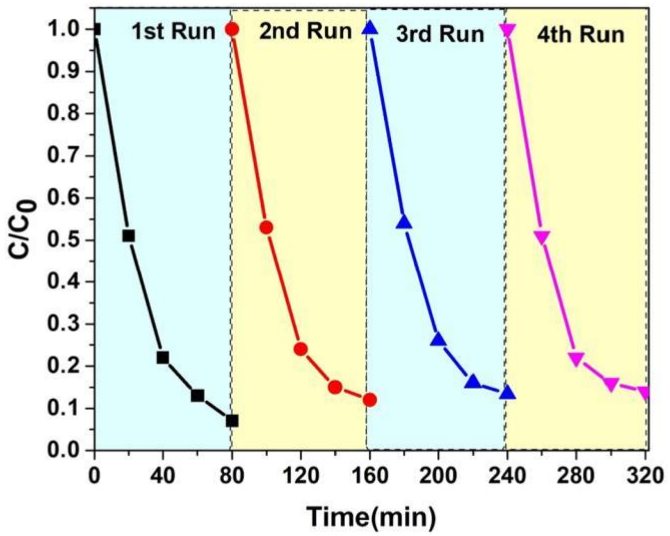

Fig. 10. Cycling runs of the photocatalytic degradation of RhB (10 ppm) over 0.15-NM@ CuS.

performance of a photocatalyst composite is directly related to the transfer rates of photogenerated electrons and holes during the photo-catalytic reaction.

The photocurrent density of the pure NH_2-MIL-101(Cr) and 0.15-NM@CuS (as the best photocatalytic sample) was also reported in Fig. 11b. The higher photocurrent density found for the 0.15-NM@CuS (0.8 $\mu A/cm^2$) sample compared to NH_2-MIL-101(Cr) (0.2 $\mu A/cm^2$) con-firms the higher photogenerated electron and hole transfer rate in the composite samples compared to pure NH_2-MIL-101(Cr), which can be associated with active electron and hole transfer between CuS and NH_2-MIL-101(Cr) in the composite sample [94].

Next, the photoluminescence (PL) spectra of the samples were de-termined (Fig. S7). The 0.15-NM@CuS sample showed a lower PL spec-trum intensity, which relates to sufficient hole and electron separation in the structure of the 0.15-NM@CuS compared to other samples. These results are consistent with the obtained data from transient pho-tocurrent and photocatalytic studies.

With the intention of further understanding of charge carrier migra-tion, EIS was recorded and presented as a Nyquist plot (Fig. 12a). The small semicircle Nyquist plots of 0.15-NM@CuS compared to NH_2-MIL-101(Cr) and CuS can be ascribed to faster electron-hole migration in the composite sample compared to the parent materials, which is consistent with the photocurrent result [95].

To further study the electrochemical behavior of the photoelectrodes, the simulated circuit of the electrochemical cell was calculated, and the electron lifetime of the 0.15-NM@CuS, NH_2-MIL-101(Cr), and CuS was estimated from a Bode plot. The corresponding parameters calculated for the equivalent circuit are presented in Table 2. The equivalent circuit consisted of two parallel R_C and C_{dl} ele-ments along with the Warburg impedance (Zw) used to fit the data (Fig. 12a inset). As shown in Fig. 12a, FTO sheet resistance (Rs) is repre-sented by a non-zero intercept on the real axis in the EIS plot. R_{CE} is the resistance of the electrode at the electrolyte interface, and R_{CT} is the re-sistance due to the charge transfer at the interface of the photoelectrode with the electrolyte. The electron lifetime was also calculated from the peak angular frequency value, which shows a higher value for 0.15-NM@CuS compared to NH_2-MIL-101(Cr) and CuS, thereby confirming the effective electron-hole separation in the composite sample [96].

The electron lifetimes are calculated from the peak angular fre-quency value (f_{max}) using the following equation:

$$\tau_n ¼ \frac{1}{2\pi f_{max}}$$

A higher τ_n value reveals that the electrons have an extended life-time and transferred efficiently, resulting in higher photocurrent den-sity with elevated energy conversion efficiency.

To determine the flat band potential of the NH_2-MIL-101(Cr) and CuS, Mott-Schottky analysis was used [97]. The positive slope of the Mott-Schottky plot (Fig. 13a) for NH_2-MIL-101(Cr) and a negative slope for the CuS nanoparticles (Fig. 13b) revealed the n-type and p-type properties of the MIL-101(Cr) and CuS nanoparticles, respectively [98]. As shown in Fig. 13(a,b), the flat band potentials (vs. Ag/AgCl) for NH_2-MIL-101(Cr) and CuS nanoparticles are located at −0.6 V and 0.85 V, respectively. The flat band potentials can be converted into nor-mal hydrogen electrode potential (NHE) according to the following equation ($E°_{Ag/AgC1}$ = 0.197 V):

$$E_{NHE} ¼ E_{Ag=AgC1} þ E_{Ag=AgC1}$$

It is commonly accepted that the potential of the conduction band (CB) is 0.1 V above the flat band in an n-type semiconductor, and the po-tential of the valence band (VB) is 0.1 V below the flat band potential in

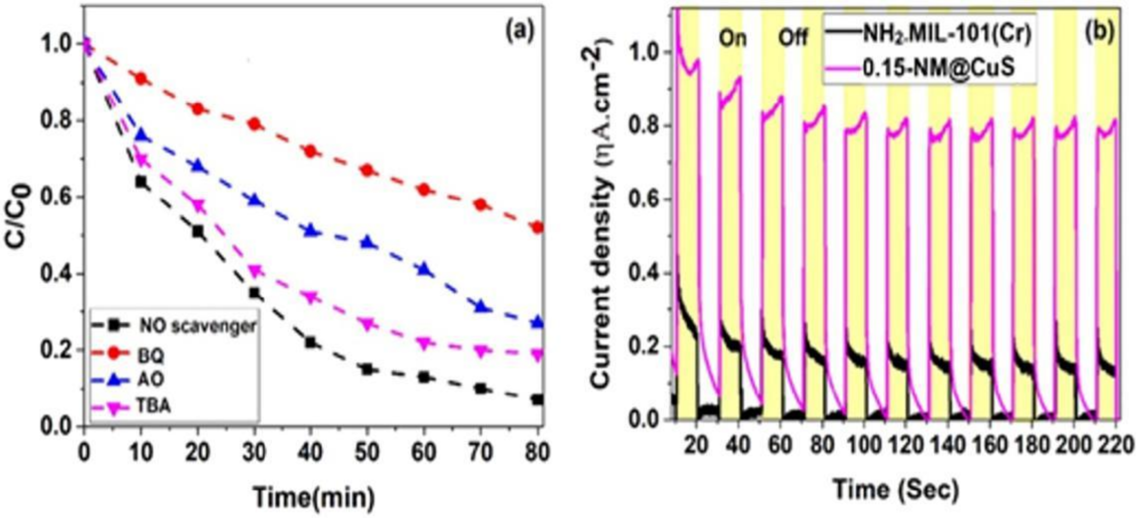

Fig. 11. (a) Photocatalytic activity of the 0.15-NM@CuS for the degradation of RhB in the presence of different scavengers, (b) transient photocurrent response of the pure NH_2-MIL-101(Cr) and 0.15-NM@CuS.

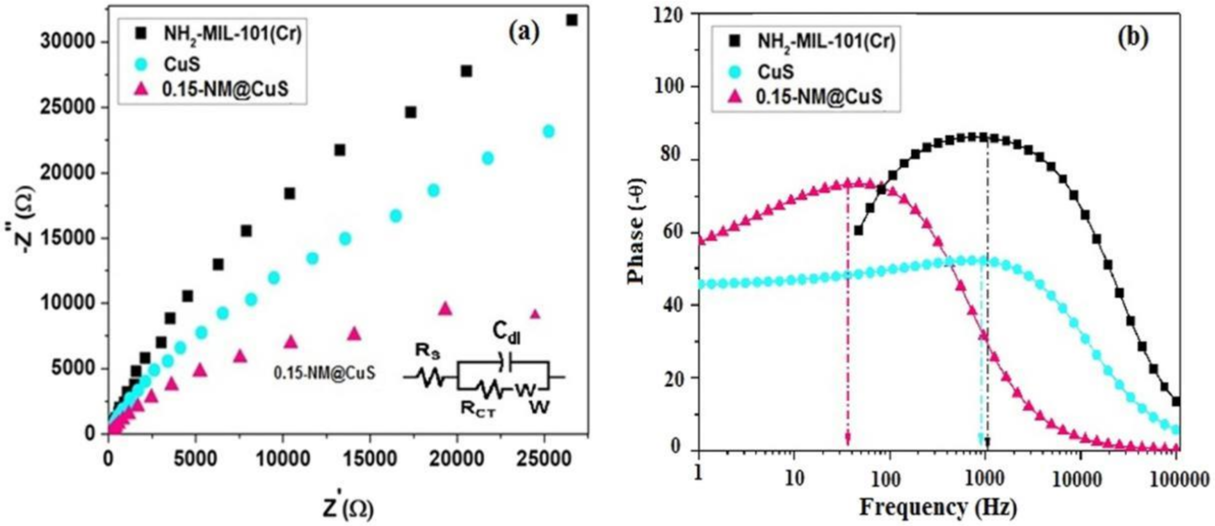

Fig. 12. (a) EIS property (Nyquist plot) of NH_2-MIL-101(Cr), CuS, and 0.15-NM@CuS composites (b) bode plot of the of NH_2-MIL-101(Cr), CuS, and 0.15-NM@CuS composite.

Table 2
The electrochemical parameters of the as-prepared photocatalytic electrode derived from the simulated circuit.

Sample	R_S (Ω)	R_{CT} (Ω)	C_{dl} (μF)	Z_W (μΩ)	$τ_n$ (ms)
CuS	117.6	0.005	11.98	15.57	0.2
NH_2-MIL-101 (Cr)	105.6	5.65	4.79	25.44	0.2
0.15-NM@CuS	82.8	0.034	5.16	43.92	3.3

a p-type semiconductor [99]. Hence, the CB of NH_2-MIL-101(Cr) and VB of CuS are −0.503 and 1.147 V (vs. NHE), respectively, with band gap potentials of 2.6 eV for NH_2-MIL-101(Cr) and 1.8 eV for CuS. Thus, the VB and CB potential of NH_2-MIL-101(Cr) and CuS are calculated as 2.097 eV and −0.653 eV, receptively.

3.4. Results from DFT calculations

The optimized cell parameters for CuS bulk were a = 3.782 Å and c = 16.290 Å, i.e. in excellent agreement with the experiment (a = 3.794 Å and c = 16.341 Å) [100] and previous ab initio studies (a = 3.791 Å and c = 16.400 Å) [76]. Geometries of the relaxed CuS bulk, CuS(001) surface, NH_2-MIL-110(Cr), and NH_2-MIL-101(Cr)@CuS(001) nanohybrid photocatalysts used in our calculations are shown in Fig. 14.

The thermodynamic stability of the NH_2-MIL-101(Cr)@CuS(001) composite can be investigated by calculating the binding energy using the following equation:

$$E_b = E_{NH2-MIL-101(Cr)@CuS(001)} - E_{CuS(001)} - E_{NH2-MIL-101(Cr)}$$

where $E_{NH2-MIL-101(Cr)@CuS(001)}$, $E_{CuS(001)}$ and $E_{NH2-MIL-101(Cr)}$ represent the total energies of the NH_2-MIL-101(Cr)@CuS(001) nanohybrid, the CuS(001) surface, and the NH_2-MIL-101(Cr), respectively. The cal-culated E_b is −3.85 eV for the NH_2-MIL-101(Cr)@CuS(001), which shows the stability of the hybrid structure thermodynamically, com-pared to its components.

To explore the nature of the interaction between NH_2-MIL-101(Cr) and the CuS (001) surface, electronic structure calculations of the NH_2-MIL-101(Cr), CuS(001) surface, and NH_2-MIL-101(Cr)/CuS (001) hybrid structure were carried out, and the results are shown in Figs. 15 and 16.

The calculated band structures show that the hybrid NH_2-MIL-101 (Cr)/CuS(001) system has a direct bandgap as large as 2.10 eV (Fig. 15). The CuS(001) surface has a direct bandgap of 1.64 eV, shown in Fig. 15b, with the valence band maximum (VBM) and the conduction band minimum (CBM) located at the Γ point. Besides, the direct bandgap for NH_2-MIL-101(Cr) is 2.65 at X high symmetry point (Fig. 15). These results are consistent with our experimental findings, confirming that CuS nanoparticles are mostly composed of CuS(001)

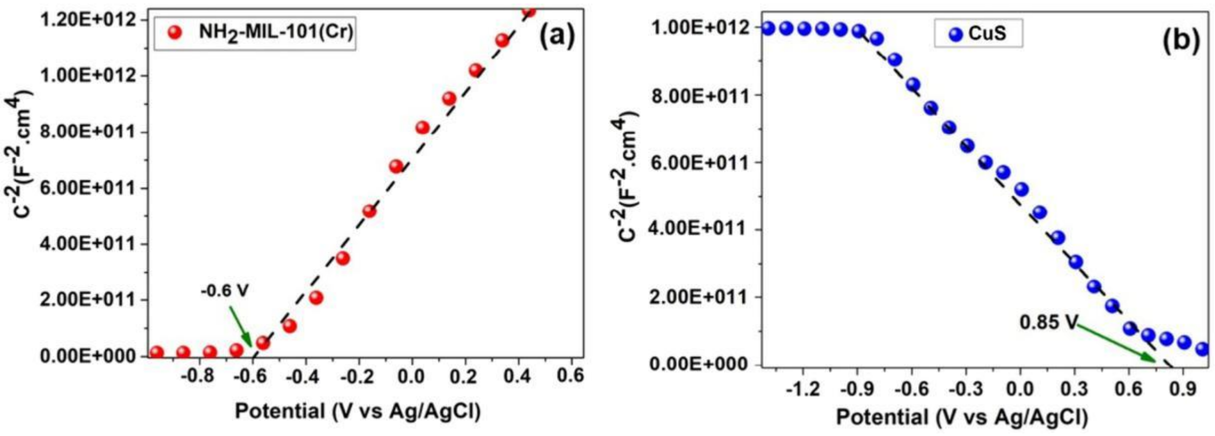

Fig. 13. Mott-Schottky plots of pure NH_2-MIL-101(Cr) and CuS.

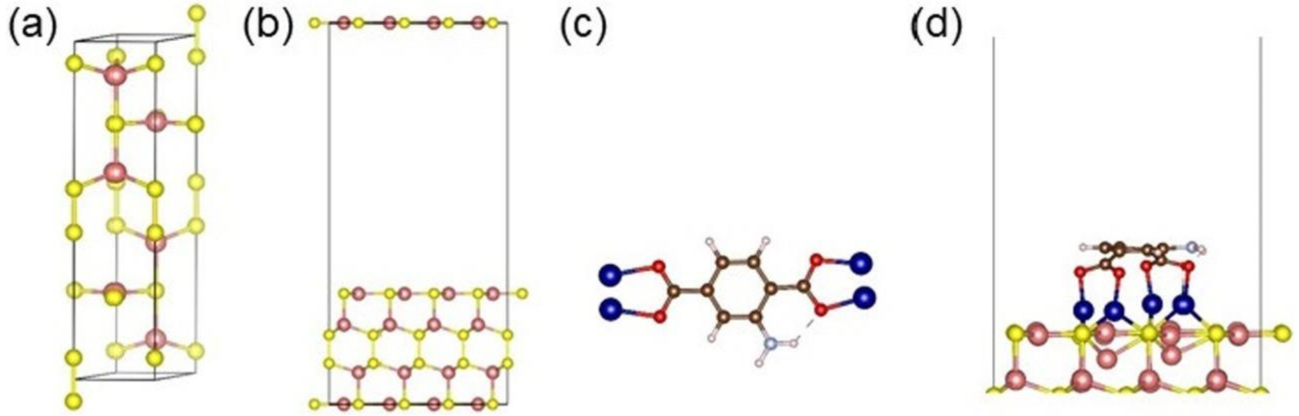

Fig. 14. Geometries of (a) CuS bulk, (b) CuS(001) surface, (c) NH_2-MIL-101(Cr) and (d) NH_2-MIL-101(Cr)@CuS(001) interface after optimization. Colors of Cu, S, O, N, H, C, and Cr atoms are pink, yellow, red, silver, white, brown, and blue, respectively. (For interpretation of the references to color in this figure legend, the reader is referred to the web version of this article.)

surfaces. It should be noted that the smaller bandgap obtained for the hybrid structure can notably increase the photocatalytic performance of NH_2-MIL-101(Cr) under visible irradiation.

To further study the electronic structure of the NH_2-MIL-101(Cr) and CuS(001) at the interface in the hybrid system, the total DOS (TDOS) and its projected DOS (PDOS) were also calculated, and the results are shown in Fig. 16. According to Fig. 16a, while the CBM of the NH_2-MIL-101(Cr)/CuS(001) hetero-structure mainly originates from the atomic orbitals Cr(p) of the NH_2-MIL-101(Cr), the VBM is dominated by the Cu(d) and S(p) orbitals of the CuS(001) surface. Moreover, Fig. 16b and c indicate that the CBM and VBM of the naked CuS(001) surface and NH_2-MIL-101(Cr) semiconductor are composed of S(p) and Cr(d) orbitals, respectively.

Taking the remarkable enhancement in charge separation based on PL and photoelectrochemical analysis, the composite photocatalyst has a direct Z-Scheme mechanism, which is shown in Scheme 1.

Visible-light irradiation drives the electrons generated in the CuS and NH_2-MIL-101(Cr) valence bands to the conduction band through the excitation process. The photo-exited electrons in the conduction band of NH_2-MIL-101(Cr) at −0.503 V (vs. NHE) react with holes in the valence band of CuS and at 1.147 V (vs. NHE). The trapping experi-ment revealed that the main active species were superoxide radicals ($\bullet O^{-}_{2}$). Therefore, the adsorbed O_2 molecules on the surface of the photocatalyst can be reduced by electrons in the CB of NH_2-MIL101 (Cr) to create the superoxide radicals ($\bullet O^{-}_{2}$), which can be active in the degradation process. Furthermore, holes remaining in the valence band of NH_2-MIL-101(Cr) can partially react with hydroxyl anions to form hydroxyl radicals.

The following photocatalytic reaction equations may occur during the degradation of RhB over NM@CuS samples:

NH_2− MIL − 101ðCrÞ þ hv þ NH_2 −MIL−101 Cr
þ e ðNH_2 −MIL−101ðCrÞÞ ð1Þ

CuS þ hv ! $h^þ$ ðCuSÞ þ $e^−$ ðCuSÞ ð2Þ

$e^−$ ðCuSÞ ! $e^−$ð NH_2−MIL−101ðCrÞÞ ð3Þ

$e^−$ þ O_2 ðadsorbedÞ ! $O_2^{\cdot −}$ ð4Þ

$h^þ$ þ H_2O ! $^{\cdot}$OH þ $H^þ$ ð5Þ

$O_2^{\cdot −}$ þ $h^þ$=$^{\cdot}$OH þ RhB !!! CO_2 þ H_2O ð6Þ

For a better evaluation of the photoactivity of the as-prepared samples during degradation, the degradation of organic dyes in the presence of several existing MOFs-based photocatalysts is summa-rized in Table 3. These data reveal that the 0.15-NM@CuS composite has an excellent photocatalytic performance towards the degrada-tion of organic dye.

4. Conclusion

In summary, a series of the NM@CuS composite photocatalyst sam-ples were fabricated via a conventional solvothermal approach. The photocatalytic elimination of RhB has demonstrated that the sample containing 0.15 g NH_2-MIL-101(Cr) in the precursor suspension ex-hibits higher photocatalytic ability compared to other samples, which can be attributed to the following factors: effective visible light absorp-tion in the composite samples compared to pure NH_2-MIL-101(Cr); higher surface area of the composite sample compared to pure CuS; thriving electron-hole transfer between p-type CuS and n-type NH_2-MIL-101(Cr) in the composite structures, as confirmed by electron life-time calculation, in comparison with pure MOF and CuS; and sulfur en-richment in the NM@CuS samples. The effective electron-hole transfer between p-CuS and n-type NH_2-MIL-101(Cr) could be related to opera-tional interaction between two components in the structure of the

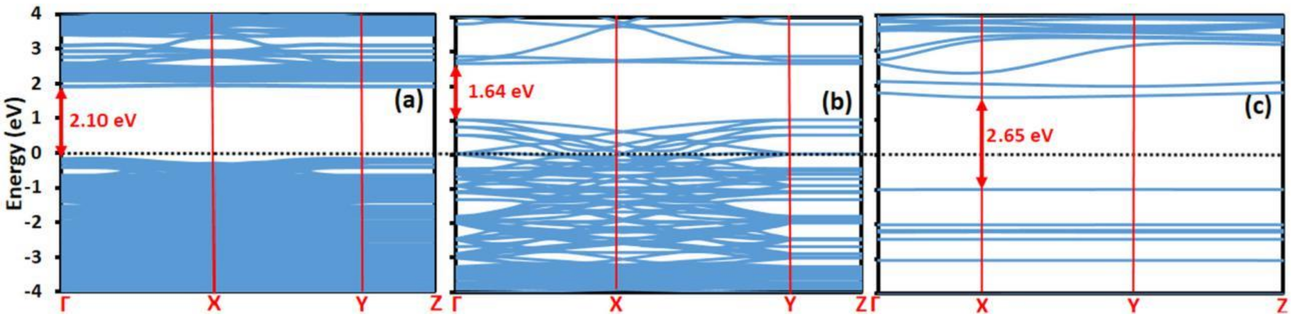

Fig. 15. Calculated band structure of (a) hybrid structure NH_2-MIL-101(Cr)@CuS(001), (b) CuS(001), and (c) NH_2-MIL-101(Cr).

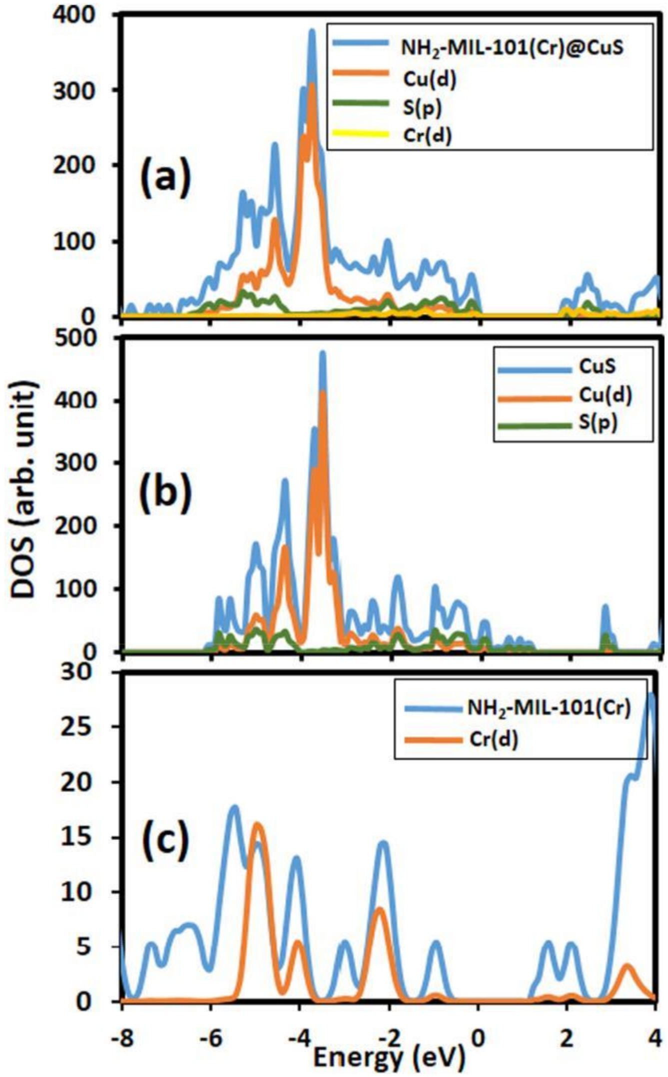

Fig. 16. Calculated DOS of (a) hybrid structure NH_2-MIL-101(Cr)@CuS(001), (b) CuS(001), and (c) NH_2-MIL-101(Cr).

composite samples, resulting from the proper potentials of the conduction and valence bands of p-CuS (CB: −0.653, VB: 1.147) to n-NH_2-MIL-101(Cr) (CB: −0.503, VB: 2.097) which forms a direct Z-scheme mechanism between the two components. The proposed mechanism based on electrochemical analysis and trapping of the reactive transient species indicated that superoxide radicals play a leading part in RhB photodegradation. The stability experiments showed the stability of the photocatalyst during the reaction. Finally, the DFT calculations confirm the band structure of the NH_2-MIL-101(Cr)@CuS nanocomposite and its components used in the experiments, showing higher photocatalytic efficiency in the visible region for the nanocomposite compared to the pristine MIL-101(Cr) and CuS. Based on the obtained results from photocatalytic experiments, electrochemical analysis, and stability tests, this work introduces the CuS nanoparticle as an efficient, low cost, and non-toxic co-catalyst for the fabrication of composite photocatalyst based on MOFs.

CRediT authorship contribution statement

Mr. Soheil Abdpour: Conceptualization Ideas, Methodology, Writing - Original Draft, Formal analysis, Investigation. **Prof. Elaheh Kowsari**: Supervision, Writing - Review & Editing. **Dr. Behrouz Bazri**: Formal analysis, Writing - Review & Editing, Investigation. **Prof. Mohammad Reza Alavi Moghaddam**: Supervision, Writing - Review & Editing. **Dr. Saeedeh SarabadaniTafreshi**: Formal analysis, simulation section. **Dr. Nora H. de Leeuw**: Formal analysis, simulation section. **Mrs. Ilka Simon**: Formal analysis. **Mrs. Laura Schmolke**: Formal analysis. **Mr. Dennis Dietrich**: Formal analysis. **Prof. Seeram Ramakrishna**: Writing - Review & Editing. **Prof. Christoph Janiak**: Writing - Review & Editing, Resources.

Declaration of competing interest

All authors have participated in (a) conception and design, or analysis and interpretation of the data; (b) drafting the article or revising it critically for important intellectual content; and (c) approval of the final version.

This manuscript has not been submitted to, nor is under review at, another journal or other publishing venue.

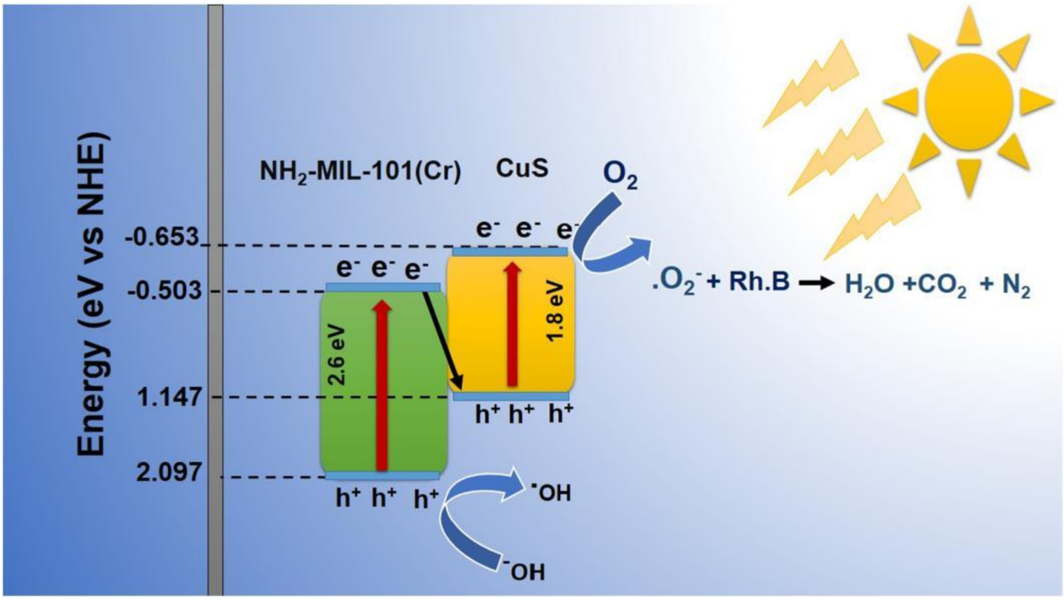

Scheme 1. Schematic illustration of the direct Z-scheme mechanism of 0.15-NM@CuS towards the photodegradation of RhB.

Table 3
Comparisons of the photocatalytic efficiency of some reported MOF based photocatalyst with the as-prepared 0.15-NM@CuS.

Photocatalyst	Dye (ppm)	Catalyst (g/L)	Removal efficiency	Irradiation time (min)	Ref.
NH_2-MIL-101(Cr)@CuS	RhB[a] (10)	0.1	94%	80	This work
TiO_2@ salicylaldehyde@NH_2-MIL-101(Cr)	MB[b] (30)	0.125	90%	90	[101]
$SrZrO_3$-MOF	Ic[c] (30)	0.4	51%	250	[102]
UiO-66(Zr)@Bi_2MoO_6	RhB (10)	0.5	94%	120	[103]
Phosphotungstic acid@MIL-53(Fe)	RhB (10)	1	98%	120	[104]
NH_2-MIL-25@Ag_3PO_4	RhB (10)	0.5	74%	30	[105]
$BiVO_4$/MIL 125(Ti)	RhB (10)	0.5	92%	180	[106]
N-TiO_2@ MIL-100(Fe)	RhB (5)	1	93.4%	180	[107]
MOF/$CuWO_4$	MB (10)	0.2	92%	150	[108]
CdS@MIL-53(Fe)	RhB (10)	1	90%	120	[109]
AgI/UiO-66(Zr)	RhB (30)	1	98%	60	[110]
Bi_2WO_6/UiO-66(Zr)	RhB (30)	0.5	98%	180	[111]
BiOBr/NH_2-MIL-125(Ti)	RhB (20)	0.2	98%	100	[112]
Ag_2CO_3/UiO-66(Zr)	RhB (30)	0.5	97%	120	[113]

[a] Rhodamine B.
[b] Methylene blue.
[c] Indigo carmine.

The authors have no affiliation with any organization with a direct or indirect financial interest in the subject matter discussed in the manuscript.

Acknowledgment

We wish to express our gratitude to the Iran National Science Foundation (INSF) (Project no. 96001364) and Research Affairs Division at the Amirkabir University of Technology of Tehran (AUT) (Grant no. 1235/40) for financial support. This work has used computational facilities of the Advanced Research Computing @ Cardiff (ARCCA) Division, Cardiff University, UK.

Appendix A. Supplementary data

FT-IR spectra of the as-prepared samples, The EDX elemental analysis of the as-prepared samples, XPS data of 0.15-NM@CuS sample, XPS spectrum of C1s, O1s, N1s of the 0.15-NM@CuS sample, PXRD patterns, and FTIR spectrum of the 0.15- NM@CuS sample before and after the photocatalytic reaction, Photoluminescence spectra of the as-prepared samples and the concentration of Cr(III) during the photocatalytic reaction.

References

[1] H. Wang, Y. Liu, M. Li, H. Huang, H.M. Xu, R.J. Hong, H. Shen, Multifunctional TiO2 nanowires-modified nanoparticles bilayer film for 3D dye-sensitized solar cells, Optoelectron. Adv. Mater. Rapid Commun. 4 (2010) 1166–1169.

[2] M. Hasanpour, M. Hatami, Photocatalytic performance of aerogels for organic dyes removal from wastewaters: review study, J. Mol. Liq. (2020), 113094, https://doi.org/10.1016/j.molliq.2020.113094.

[3] S.B. Bagherzadeh, M. Kazemeini, N.M. Mahmoodi, A study of the DR23 dye photocatalytic degradation utilizing a magnetic hybrid nanocomposite of MIL-53(Fe)/CoFe2O4: facile synthesis and kinetic investigations, J. Mol. Liq. 301 (2020), 112427, https://doi.org/10.1016/j.molliq.2019.112427.

[4] A.M. Awad, R. Jalab, A. Benamor, M.S. Nasser, M.M. Ba-Abbad, M. El-Naas, A.W. Mohammad, Adsorption of organic pollutants by nanomaterial-based adsorbents: an overview, J. Mol. Liq. 301 (2020), 112335, https://doi.org/10.1016/j.molliq.2019.112335.

[5] N.M. Mahmoodi, M. Oveisi, M. Bakhtiari, B. Hayati, A.A. Shekarchi, A. Bagheri, S. Rahimi, Environmentally friendly ultrasound-assisted synthesis of magnetic zeolitic imidazolate framework - graphene oxide nanocomposites and pollutant removal from water, J. Mol. Liq. 282 (2019) 115–130, https://doi.org/10.1016/j.molliq.2019.02.139.

[6] M.M. Ba-Abbad, M.S. Takriff, A.A.H. Kadhum, A.B. Mohamad, A. Benamor, A.W. Mohammad, Solar photocatalytic degradation of 2-chlorophenol with ZnO nanoparticles: optimisation with D-optimal design and study of intermediate mechanisms, Environ. Sci. Pollut. Res. 24 (2017) 2804–2819, https://doi.org/10.1007/s11356-016-8033-y.

[7] M.M. Ba-Abbad, M.S. Takriff, A. Benamor, A.W. Mohammad, Size and shape controlled of α-Fe2O3 nanoparticles prepared via sol–gel technique and their photocatalytic activity, J. Sol-Gel Sci. Technol. 81 (2017) 880–893, https://doi.org/10.1007/s10971-016-4228-4.

[8] W. Zhang, R.Z. Zhang, Y. Yin, J.M. Yang, Superior selective adsorption of anionic organic dyes by MIL-101 analogs: regulation of adsorption driving forces by free amino groups in pore channels, J. Mol. Liq. 302 (2020), 112616, https://doi.org/10.1016/j.molliq.2020.112616.

[9] S. Liang, D. Zhang, X. Pu, X. Yao, R. Han, J. Yin, X. Ren, A novel Ag2O/g-C3N4 p-n heterojunction photocatalysts with enhanced visible and near-infrared light activity, Sep. Purif. Technol. 210 (2019) 786–797, https://doi.org/10.1016/j.seppur.2018.09.008.

[10] Y. Wu, P. Wang, X. Zhu, Q. Zhang, Z. Wang, Y. Liu, G. Zou, Y. Dai, M.-H. Whangbo, B. Huang, Composite of CH3NH3PbI3 with reduced graphene oxide as a highly efficient and stable visible-light photocatalyst for hydrogen evolution in aqueous HI solution, Adv. Mater. 30 (2018), 1704342, https://doi.org/10.1002/adma.201704342.

[11] X. Wang, X. Wang, J. Song, Y. Li, Z. Wang, Y. Gao, A highly efficient TiOX (X = N and P) photocatalyst for inactivation of Microcystis aeruginosa under visible light irradiation, Sep. Purif. Technol. 222 (2019) 99–108, https://doi.org/10.1016/j.seppur.2019.04.034.

[12] T. Zhang, M. Liu, Y. Meng, B. Huang, X. Pu, X. Shao, A novel method for the synthesis of Ag3VO4/Ag2VO2PO4 heterojunction photocatalysts with improved visible-light photocatalytic properties, Sep. Purif. Technol. 206 (2018) 149–157, https://doi.org/10.1016/j.seppur.2018.05.068.

[13] M. Jahanshahi, E. Kowsari, V. Haddadi-Asl, M. Khoobi, B. Bazri, M. Aryafard, J.H. Lee, F.B. Kadumudi, S. Talebian, N. Kamaly, M. Mehrali, A. Dolatshahi-Pirouz, An innovative and eco-friendly modality for synthesis of highly fluorinated graphene by an acidic ionic liquid: making of an efficacious vehicle for anti-cancer drug delivery, Appl. Surf. Sci. 515 (2020), 146071, https://doi.org/10.1016/j.apsusc.2020.146071.

[14] M. Jahanshahi, E. Kowsari, V. Haddadi-Asl, M. Khoobi, J.H. Lee, F.B. Kadumudi, S. Talebian, N. Kamaly, M. Mehrali, Sericin grafted multifunctional curcumin loaded fluorinated graphene oxide nanomedicines with charge switching properties for effective cancer cell targeting, Int. J. Pharm. 572 (2019), 118791, https://doi.org/10.1016/j.ijpharm.2019.118791.

[15] R. Liang, F. Jing, L. Shen, N. Qin, L. Wu, MIL-53(Fe) as a highly efficient bifunctional photocatalyst for the simultaneous reduction of Cr(VI) and oxidation of dyes, J. Hazard. Mater. 287 (2015) 364–372, https://doi.org/10.1016/j.jhazmat.2015.01.048.

[16] J. Qiu, X.-F. Zhang, X. Zhang, Y. Feng, Y. Li, L. Yang, H. Lu, J. Yao, Constructing Cd0.5Zn0.5S@ZIF-8 nanocomposites through self-assembly strategy to enhance Cr(VI) photocatalytic reduction, J. Hazard. Mater. 349 (2018) 234–241, https://doi.org/10.1016/j.jhazmat.2018.02.009.

[17] Q. Gong, Y. Liu, Z. Dang, Core-shell structured Fe3O4@GO@MIL-100(Fe) magnetic nanoparticles as heterogeneous photo-Fenton catalyst for 2,4-dichlorophenol degradation under visible light, J. Hazard. Mater. 371 (2019) 677–686, https://doi.org/10.1016/j.jhazmat.2019.03.019.

[18] Y. Zeng, N. Guo, Y. Song, Y. Zhao, H. Li, X. Xu, J. Qiu, H. Yu, Fabrication of Z-scheme magnetic MoS2/CoFe2O4 nanocomposites with highly efficient photocatalytic activity, J. Colloid Interface Sci. 514 (2018) 664–674, https://doi.org/10.1016/j.jcis.2017.12.079.

[19] S. Li, J. Cui, X. Wu, X. Zhang, Q. Hu, X. Hou, Rapid in situ microwave synthesis of Fe3O4@MIL-100(Fe) for aqueous diclofenac sodium removal through integrated adsorption and photodegradation, J. Hazard. Mater. 373 (2019) 408–416, https://doi.org/10.1016/j.jhazmat.2019.03.102.

[20] Y. Deng, L. Tang, C. Feng, G. Zeng, Z. Chen, J. Wang, H. Feng, B. Peng, Y. Liu, Y. Zhou, Insight into the dual-channel charge-charrier transfer path for nonmetal plasmonic tungsten oxide based composites with boosted photocatalytic activity under full-spectrum light, Appl. Catal. B Environ. 235 (2018) 225–237, https://doi.org/10.1016/j.apcatb.2018.04.075.

[21] Y. Deng, C. Feng, L. Tang, Y. Zhou, Z. Chen, H. Feng, J. Wang, J. Yu, Y. Liu, Ultrathin low dimensional heterostructure composites with superior photocatalytic activity:

insight into the multichannel charge transfer mechanism, Chem. Eng. J. 393 (2020) 124718, https://doi.org/10.1016/j.cej.2020.124718.

[22] Y. Deng, L. Tang, G. Zeng, Z. Zhu, M. Yan, Y. Zhou, J. Wang, Y. Liu, J. Wang, Insight into highly efficient simultaneous photocatalytic removal of Cr(VI) and 2,4-diclorophenol under visible light irradiation by phosphorus doped porous ultrathin g-C3N4 nanosheets from aqueous media: performance and reaction mechanism, Appl. Catal. B Environ. 203 (2017) 343–354, https://doi.org/10.1016/j.apcatb. 2016.10.046.

[23] Y. Deng, Z. Li, R. Tang, K. Ouyang, C. Liao, Y. Fang, C. Ding, L. Yang, L. Su, D. Gong, What will happen when microorganisms "meet" photocatalysts and photocatalysis? Environ. Sci. Nano. 7 (2020) 702–723, https://doi.org/10.1039/ c9en01318k.

[24] H. Heydari, S.E. Moosavifard, S. Elyasi, M. Shahraki, Nanoporous CuS nano-hollow spheres as advanced material for high-performance supercapacitors, Appl. Surf. Sci. 394 (2017) 425–430, https://doi.org/10.1016/j.apsusc.2016.10.138.

[25] B. Zeng, X. Chen, C. Chen, X. Ning, W. Deng, Reduced graphene oxides loaded-ZnS/ CuS heteronanostructures as high-activity visible-light-driven photocatalysts, J. Al-loys Compd. 582 (2014) 774–779, https://doi.org/10.1016/j.jallcom.2013.08.121.

[26] X.-S. Hu, Y. Shen, L.-H. Xu, L.-M. Wang, Y.-J. Xing, Preparation of flower-like CuS by solvothermal method and its photodegradation and UV protection, J. Alloys Compd. 674 (2016) 289–294, https://doi.org/10.1016/j.jallcom.2016.03.047.

[27] M. Xin, K. Li, H. Wang, Synthesis of CuS thin films by microwave assisted chemical bath deposition, Appl. Surf. Sci. 256 (2009) 1436–1442, https://doi.org/10.1016/j. apsusc.2009.08.104.

[28] H. Lee, B.S. Kwak, N.-K. Park, J.-I. Baek, H.-J. Ryu, M. Kang, Assembly of a check-patterned CuSx–TiO2 film with an electron-rich pool and its application for the photoreduction of carbon dioxide to methane, Appl. Surf. Sci. 393 (2017) 385–396, https://doi.org/10.1016/j.apsusc.2016.10.026.

[29] J. Wu, B. Liu, Z. Ren, M. Ni, C. Li, Y. Gong, W. Qin, Y. Huang, C.Q. Sun, X. Liu, CuS/RGO hybrid photocatalyst for full solar spectrum photoreduction from UV/Vis to near-infrared light, J. Colloid Interface Sci. 517 (2018) 80–85, https://doi.org/10.1016/j. jcis.2017.09.042.

[30] G. Heidari, M. Rabani, B. Ramezanzadeh, Application of CuS–ZnS PN junction for photoelectrochemical water splitting, Int. J. Hydrog. Energy 42 (2017) 9545–9552, https://doi.org/10.1016/j.ijhydene.2017.01.176.

[31] X. Wang, L. Li, Z. Fu, F. Cui, Carbon quantum dots decorated CuS nanocomposite for effective degradation of methylene blue and antibacterial performance, J. Mol. Liq. 268 (2018) 578–586, https://doi.org/10.1016/j.molliq.2018.07.086.

[32] M. Saranya, C. Santhosh, R. Ramachandran, P. Kollu, P. Saravanan, M. Vinoba, S.K. Jeong, A.N. Grace, Hydrothermal growth of CuS nanostructures and its photocata-lytic properties, Powder Technol. 252 (2014) 25–32, https://doi.org/10.1016/j. powtec.2013.10.031.

[33] W. Liu, H. Ji, J. Wang, X. Zheng, J. Lai, J. Ji, T. Li, Y. Ma, H. Li, S. Zhao, Z. Jin, Synthesis and photo-response of CuS thin films by an in situ multi-deposition process at room temperature: a facile and eco-friendly approach, Nano 10 (2015), 1550032, https://doi.org/10.1142/S1793292015500320.

[34] X. Chen, H. Li, Y. Wu, H. Wu, L. Wu, P. Tan, J. Pan, X. Xiong, Facile fabrication of novel porous graphitic carbon nitride/copper sulfide nanocomposites with en-hanced visible light driven photocatalytic performance, J. Colloid Interface Sci. 476 (2016) 132–143, https://doi.org/10.1016/j.jcis.2016.05.024.

[35] N. Karikalan, R. Karthik, S.-M. Chen, C. Karuppiah, A. Elangovan, Sonochemical syn-thesis of sulfur doped reduced graphene oxide supported CuS nanoparticles for the non-enzymatic glucose sensor applications, Sci. Rep. 7 (2017) 2494, https://doi. org/10.1038/s41598-017-02479-5.

[36] X.-S. Hu, Y. Shen, Y.-T. Zhang, J.-J. Nie, Preparation of flower-like CuS/reduced graphene oxide(RGO) photocatalysts for enhanced photocatalytic activity, J. Phys. Chem. Solids 103 (2017) 201–208, https://doi.org/10.1016/j.jpcs.2016.12. 021.

[37] F. Rashidi, E. Lima, H. Rashidi, A. Rashidi, A. Guzmán, Cooperative effect of gold nanoparticles with CUS aluminium from nanoalumina support in the catalysis of an electron transfer reaction, Appl. Catal. A Gen. 417–418 (2012) 129–136, https://doi.org/10.1016/j.apcata.2011.12.032.

[38] J. Zhang, Z. Xiong, C. Li, C. Wu, Exploring a thiol-functionalized MOF for elimination of lead and cadmium from aqueous solution, J. Mol. Liq. 221 (2016) 43–50, https:// doi.org/10.1016/j.molliq.2016.05.054.

[39] Z. Huang, M. Zhao, S. Wang, L. Dai, L. Zhang, C. Wang, Selective recovery of gold ions in aqueous solutions by a novel trithiocyanuric-Zr based MOFs adsorbent, J. Mol. Liq. 298 (2020), 112090, https://doi.org/10.1016/j.molliq.2019.112090.

[40] A.M. Ghaedi, M. Panahimehr, A.R.S. Nejad, S.J. Hosseini, A. Vafaei, M.M. Baneshi, Factorial experimental design for the optimization of highly selective adsorption removal of lead and copper ions using metal organic framework MOF-2 (Cd), J. Mol. Liq. 272 (2018) 15–26, https://doi.org/10.1016/j.molliq.2018.09.051.

[41] A.J. Sisi, A. Khataee, M. Fathinia, B. Vahid, Ultrasonic-assisted degradation of a triarylmethane dye using combined peroxydisulfate and MOF-2 catalyst: synergis-tic effect and role of oxidative species, J. Mol. Liq. 297 (2020), 111838, https://doi. org/10.1016/j.molliq.2019.111838.

[42] N.M. Mahmoodi, S. Keshavarzi, M. Oveisi, S. Rahimi, B. Hayati, Metal-organic framework (ZIF-8)/inorganic nanofiber (Fe2O3) nanocomposite: green synthesis and photocatalytic degradation using LED irradiation, J. Mol. Liq. 291 (2019), 111333, https://doi.org/10.1016/j.molliq.2019.111333.

[43] M.R. Delsouz Khaki, M.S. Shafeeyan, A.A.A. Raman, W.M.A.W. Daud, Evaluating the efficiency of nano-sized Cu doped TiO2/ZnO photocatalyst under visible light irra-diation, J. Mol. Liq. 258 (2018) 354–365, https://doi.org/10.1016/j.molliq.2017.11. 030.

[44] J.-M. Yang, X.-W. Hu, Y.-X. Liu, W. Zhang, Fabrication of a carbon quantum dots-immobilized zirconium-based metal-organic framework composite fluorescence sensor for highly sensitive detection of 4-nitrophenol, Microporous Mesoporous Mater. 274 (2019) 149–154, https://doi.org/10.1016/j.micromeso.2018.07.042.

[45] M. Alvaro, E. Carbonell, B. Ferrer, F.X. Llabrés i Xamena, H. Garcia, Semiconductor behavior of a metal-organic framework (MOF), Chem. - A Eur. J. 13 (2007) 5106–5112, https://doi.org/10.1002/chem.200601003.

[46] Y. Pi, X. Li, Q. Xia, J. Wu, Y. Li, J. Xiao, Z. Li, Adsorptive and photocatalytic removal of persistent organic pollutants (POPs) in water by metal-organic frameworks (MOFs), Chem. Eng. J. 337 (2018) 351–371, https://doi.org/10.1016/j.cej.2017.12. 092.

[47] D.Y. Lee, D.V. Shinde, S.J. Yoon, K.N. Cho, W. Lee, N.K. Shrestha, S.-H. Han, Cu-based metal–organic frameworks for photovoltaic application, J. Phys. Chem. C 118 (2014) 16328–16334, https://doi.org/10.1021/jp4079663.

[48] D.Y. Ahn, D.Y. Lee, C.Y. Shin, H.T. Bui, N.K. Shrestha, L. Giebeler, Y.-Y. Noh, S.-H. Han, Novel solid-state solar cell based on hole-conducting MOF-sensitizer demonstrat-ing power conversion efficiency of 2.1%, ACS Appl. Mater. Interfaces 9 (2017) 12930–12935, https://doi.org/10.1021/acsami.7b03487.

[49] Y. Wang, Y. Zhang, Z. Jiang, G. Jiang, Z. Zhao, Q. Wu, Y. Liu, Q. Xu, A. Duan, C. Xu, Controlled fabrication and enhanced visible-light photocatalytic hydrogen produc-tion of Au@CdS/MIL-101 heterostructure, Appl. Catal. B Environ. 185 (2016) 307–314, https://doi.org/10.1016/j.apcatb.2015.12.020.

[50] S. Rahim Pouran, A. Bayrami, A.R. Abdul Aziz, W.M.A. Wan Daud, M.S. Shafeeyan, Ultrasound and UV assisted Fenton treatment of recalcitrant wastewaters using transition metal-substituted-magnetite nanoparticles, J. Mol. Liq. 222 (2016) 1076–1084, https://doi.org/10.1016/j.molliq.2016.07.120.

[51] M.R. Delsouz Khaki, M.S. Shafeeyan, A.A.A. Raman, W.M.A.W. Daud, Enhanced UV– visible photocatalytic activity of Cu-doped ZnO/TiO2 nanoparticles, J. Mater. Sci. Mater. Electron. 29 (2018) 5480–5495, https://doi.org/10.1007/s10854-017-8515-9.

[52] M. Oveisi, M.A. Asli, N.M. Mahmoodi, MIL-Ti metal-organic frameworks (MOFs) nanomaterials as superior adsorbents: synthesis and ultrasound-aided dye adsorp-tion from multicomponent wastewater systems, J. Hazard. Mater. 347 (2018) 123–140, https://doi.org/10.1016/j.jhazmat.2017.12.057.

[53] S. Abdpour, E. Kowsari, M.R.A. Moghaddam, Synthesis of MIL-100(Fe)@MIL-53(Fe) as a novel hybrid photocatalyst and evaluation photocatalytic and photoelectrochemical performance under visible light irradiation, J. Solid State Chem. 262 (2018) 172–180, https://doi.org/10.1016/j.jssc.2018.03.018.

[54] N.M. Mahmoodi, J. Abdi, Nanoporous metal-organic framework (MOF-199): syn-thesis, characterization and photocatalytic degradation of Basic Blue 41, Microchem. J. 144 (2019) 436–442, https://doi.org/10.1016/j.microc.2018.09.033.

[55] J. Yu, S. Wang, J. Low, W. Xiao, Enhanced photocatalytic performance of direct Z-scheme g-C3N4–TiO2 photocatalysts for the decomposition of formaldehyde in air, Phys. Chem. Chem. Phys. 15 (2013), 16883, https://doi.org/10.1039/ c3cp53131g.

[56] J. He, Z. Yan, J. Wang, J. Xie, L. Jiang, Y. Shi, F. Yuan, F. Yu, Y. Sun, Significantly en-hanced photocatalytic hydrogen evolution under visible light over CdS embedded on metal–organic frameworks, Chem. Commun. 49 (2013) 6761, https://doi.org/ 10.1039/c3cc43218a.

[57] S. Abdpour, E. Kowsari, M.R. Alavi Moghaddam, L. Schmolke, C. Janiak, Mil-100(Fe) nanoparticles supported on urchin like Bi2S3 structure for improving photocata-lytic degradation of rhodamine-B dye under visible light irradiation, J. Solid State Chem. 266 (2018) 54–62, https://doi.org/10.1016/j.jssc.2018.07.006.

[58] W. Zhan, Q. Kuang, J. Zhou, X. Kong, Z. Xie, L. Zheng, Semiconductor@metal–or-ganic framework core–shell heterostructures: a case of ZnO@ZIF-8 nanorods with selective photoelectrochemical response, J. Am. Chem. Soc. 135 (2013) 1926–1933, https://doi.org/10.1021/ja311085e.

[59] A. Crake, K.C. Christoforidis, A. Kafizas, S. Zafeiratos, C. Petit, CO2 capture and pho-tocatalytic reduction using bifunctional TiO2/MOF nanocomposites under UV–vis irradiation, Appl. Catal. B Environ. 210 (2017) 131–140, https://doi.org/10.1016/j. apcatb.2017.03.039.

[60] Y. Zhang, D. Lan, Y. Wang, H. Cao, H. Jiang, MOF-5 decorated hierarchical ZnO nano-rod arrays and its photoluminescence, Phys. E Low-Dimensional Syst. Nanostruc-tures 43 (2011) 1219–1223, https://doi.org/10.1016/j.physe.2011.02.004.

[61] Y. Cui, L. Nengzi, J. Gou, Y. Huang, B. Li, X. Cheng, Fabrication of dual Z-scheme MIL-53(Fe)/α-Bi2O3/g-C3N4 ternary composite with enhanced visible light photocata-lytic performance, Sep. Purif. Technol. 232 (2020), 115959, https://doi.org/10. 1016/j.seppur.2019.115959.

[62] Q. Xu, L. Zhang, J. Yu, S. Wageh, A.A. Al-Ghamdi, M. Jaroniec, Direct Z-scheme photocatalysts: principles, synthesis, and applications, Mater. Today 21 (2018) 1042–1063, https://doi.org/10.1016/j.mattod.2018.04.008.

[63] A. Khutia, H.U. Rammelberg, T. Schmidt, S. Henninger, C. Janiak, Water sorption cycle measurements on functionalized MIL-101Cr for heat transformation applica-tion, Chem. Mater. 25 (2013) 790–798, https://doi.org/10.1021/cm304055k.

[64] F. Li, J. Wu, Q. Qin, Z. Li, X. Huang, Controllable synthesis, optical and photocatalytic properties of CuS nanomaterials with hierarchical structures, Powder Technol. 198 (2010) 267–274, https://doi.org/10.1016/j.powtec.2009.11.018.

[65] B. Bazri, E. Kowsari, N. Seifvand, N. Naseri, RGO-α-Fe2O3/β-FeOOH ternary heterostructure with urchin-like morphology for efficient oxygen evolution reac-tion, J. Electroanal. Chem. 843 (2019) 1–11, https://doi.org/10.1016/j.jelechem. 2019.04.069.

[66] P. Hohenberg, W. Kohn, Inhomogeneous electron gas, Phys. Rev. 136 (1964) B864–B871, https://doi.org/10.1103/PhysRev.136.B864.

[67] W. Kohn, L.J. Sham, Self-consistent equations including exchange and correlation effects, Phys. Rev. 140 (1965) A1133–A1138, https://doi.org/10.1103/PhysRev. 140.A1133.

[68] G. Kresse, J. Furthmüller, Efficiency of ab-initio total energy calculations for metals and semiconductors using a plane-wave basis set, Comput. Mater. Sci. 6 (1996) 15–50, https://doi.org/10.1016/0927-0256(96)00008-0.

[69] G. Kresse, J. Furthmüller, Efficient iterative schemes for ab initio total-energy calculations using a plane-wave basis set, Phys. Rev. B 54 (1996) 11169–11186, https://doi.org/10.1103/PhysRevB.54.11169.

[70] J.P. Perdew, K. Burke, M. Ernzerhof, Generalized gradient approximation made sim-ple, Phys. Rev. Lett. 77 (1996) 3865–3868, https://doi.org/10.1103/PhysRevLett.77. 3865.

[71] P.E. Blöchl, Projector augmented-wave method, Phys. Rev. B 50 (1994) 17953–17979, https://doi.org/10.1103/PhysRevB.50.17953.

[72] S.S. Tafreshi, A. Roldan, N.H. de Leeuw, Density functional theory study of the adsorption of hydrazine on the perfect and defective copper (100), (110), and (111) surfaces, J. Phys. Chem. C 118 (2014) 26103–26114, https://doi.org/10.1021/jp5078664.

[73] S. Grimme, S. Ehrlich, L. Goerigk, Effect of the damping function in dispersion corrected density functional theory, J. Comput. Chem. 32 (2011) 1456–1465, https://doi.org/10.1002/jcc.21759.

[74] J. Paier, R. Hirschl, M. Marsman, G. Kresse, The Perdew–Burke–Ernzerhof exchange-correlation functional applied to the G2-1 test set using a plane-wave basis set, J. Chem. Phys. 122 (2005), 234102, https://doi.org/10.1063/1.1926272.

[75] X. Wu, I. Choudhuri, D.G. Truhlar, Computational studies of photocatalysis with metal–organic frameworks, ENERGY Environ. Mater. 2 (2019) 251–263, https://doi.org/10.1002/eem2.12051.

[76] Á. Morales-García, J. He, A.L. Soares, H.A. Duarte, Surfaces and morphologies of covellite (CuS) nanoparticles by means of ab initio atomistic thermodynamics, CrystEngComm 19 (2017) 3078–3084, https://doi.org/10.1039/C7CE00203C.

[77] H.J. Monkhorst, J.D. Pack, Special points for Brillouin-zone integrations, Phys. Rev. B 13 (1976) 5188–5192, https://doi.org/10.1103/PhysRevB.13.5188.

[78] X. Huang, J. Lu, W. Wang, X. Wei, J. Ding, Experimental and computational investigation of CO2 capture on amine grafted metal-organic framework NH2-MIL-101, Appl. Surf. Sci. 371 (2016) 307–313, https://doi.org/10.1016/j.apsusc.2016.02.154.

[79] D. Jiang, L.L. Keenan, A.D. Burrows, K.J. Edler, Synthesis and post-synthetic modification of MIL-101(Cr)-NH2via a tandem diazotisation process, Chem. Commun. 48 (2012), 12053, https://doi.org/10.1039/c2cc36344e.

[80] M. Venkata-Haritha, C.V.V.M. Gopi, L. Young-Seok, H.-J. Kim, Controlled growth of a nanoplatelet-structured copper sulfide thin film as a highly efficient counter elec-trode for quantum dot-sensitized solar cells, RSC Adv. 6 (2016) 45809–45818, https://doi.org/10.1039/C6RA08375G.

[81] H.-J. Kim, L. Myung-Sik, C.V.V.M. Gopi, M. Venkata-Haritha, S.S. Rao, S.-K. Kim, Cost-effective and morphology controllable PVP based highly efficient CuS counter elec-trodes for high-efficiency quantum dot-sensitized solar cells, Dalton Trans. 44 (2015) 11340–11351, https://doi.org/10.1039/C5DT01412C.

[82] X.-L. Yu, C.-B. Cao, H.-S. Zhu, Q.-S. Li, C.-L. Liu, Q.-H. Gong, Nanometer-sized copper sulfide hollow spheres with strong optical-limiting properties, Adv. Funct. Mater. 17 (2007) 1397–1401, https://doi.org/10.1002/adfm.200600245.

[83] S.H. Chaki, J.P. Tailor, M.P. Deshpande, Covellite CuS – single crystal growth by chemical vapour transport (CVT) technique and characterization, Mater. Sci. Semicond. Process. 27 (2014) 577–585, https://doi.org/10.1016/j.mssp.2014.07. 038.

[84] M.C. Biesinger, B.P. Payne, A.P. Grosvenor, L.W.M. Lau, A.R. Gerson, R.S.C. Smart, Re-solving surface chemical states in XPS analysis of first row transition metals, oxides and hydroxides: Cr, Mn, Fe, Co and Ni, Appl. Surf. Sci. 257 (2011) 2717–2730, https://doi.org/10.1016/j.apsusc.2010.10.051.

[85] M.C. Biesinger, B.R. Hart, R. Polack, B.A. Kobe, R.S.C. Smart, Analysis of mineral surface chemistry in flotation separation using imaging XPS, Miner. Eng. 20 (2007) 152–162, https://doi.org/10.1016/j.mineng.2006.08.006.

[86] C. Song, X. Wang, J. Zhang, X. Chen, C. Li, Enhanced performance of direct Z-scheme CuS-WO3 system towards photocatalytic decomposition of organic pollutants under visible light, Appl. Surf. Sci. 425 (2017) 788–795, https://doi.org/10.1016/j.apsusc.2017.07.082.

[87] M. Wen, K. Mori, T. Kamegawa, H. Yamashita, Amine-functionalized MIL-101(Cr) with imbedded platinum nanoparticles as a durable photocatalyst for hydrogen production from water, Chem. Commun. 50 (2014) 11645–11648, https://doi.org/10.1039/C4CC02994A.

[88] P. Zhang, L. Gao, Copper sulfide flakes and nanodisks, J. Mater. Chem. 13 (2003) 2007, https://doi.org/10.1039/b305584a.

[89] C. Ratanatawanate, A. Bui, K. Vu, K.J. Balkus, Low-temperature synthesis of copper (II) sulfide quantum dot decorated TiO 2 nanotubes and their photocatalytic prop-erties, J. Phys. Chem. C 115 (2011) 6175–6180, https://doi.org/10.1021/jp109716q.

[90] J.P. Park, J.H. Heo, S.H. Im, S.-W. Kim, Highly efficient solid-state mesoscopic PbS with embedded CuS quantum dot-sensitized solar cells, J. Mater. Chem. A 4 (2016) 785–790, https://doi.org/10.1039/C5TA08668J.

[91] Z. Chen, H. Jiang, W. Jin, C. Shi, Enhanced photocatalytic performance over Bi4Ti3O12 nanosheets with controllable size and exposed {0 0 1} facets for rhoda-mine B degradation, Appl. Catal. B Environ. 180 (2016) 698–706, https://doi.org/10.1016/j.apcatb.2015.07.022.

[92] V. Augugliaro, C. Baiocchi, A. Bianco Prevot, E. García-López, V. Loddo, S. Malato, G. Marcí, L. Palmisano, M. Pazzi, E. Pramauro, Azo-dyes photocatalytic degradation in aqueous suspension of TiO2 under solar irradiation, Chemosphere 49 (2002) 1223–1230, https://doi.org/10.1016/S0045-6535(02)00489-7.

[93] M. Dorraj, M. Alizadeh, N.A. Sairi, W.J. Basirun, B.T. Goh, P.M. Woi, Y. Alias, Enhanced visible light photocatalytic activity of copper-doped titanium oxide–zinc oxide heterojunction for methyl orange degradation, Appl. Surf. Sci. 414 (2017) 251–261, https://doi.org/10.1016/j.apsusc.2017.04.045.

[94] W. Zhao, Y. Liu, Z. Wei, S. Yang, H. He, C. Sun, Fabrication of a novel p−n heterojunction photocatalyst n-BiVO4@p-MoS2 with core−shell structure and its excellent visible-light photocatalytic reduction and oxidation activities, Appl. Catal. B Environ. 185 (2016) 242–252, https://doi.org/10.1016/j.apcatb.2015.12. 023.

[95] M. Yan, Y. Hua, F. Zhu, W. Gu, J. Jiang, H. Shen, W. Shi, Fabrication of nitrogen doped graphene quantum dots-BiOI/MnNb2O6 p-n junction photocatalysts with en-hanced visible light efficiency in photocatalytic degradation of antibiotics, Appl. Catal. B Environ. 202 (2017) 518–527, https://doi.org/10.1016/j.apcatb.2016.09. 039.

[96] C. Venkata Thulasi-Varma, S.S. Rao, C.S.S.P. Kumar, C.V.V.M. Gopi, I.K. Durga, S.K. Kim, D. Punnoose, H.J. Kim, Enhanced photovoltaic performance and time varied controllable growth of a CuS nanoplatelet structured thin film and its application as an efficient counter electrode for quantum dot-sensitized solar cells via a cost-effective chemical bath deposition, Dalton Trans. 44 (2015) 19330–19343, https://doi.org/10.1039/c5dt02182k.

[97] P.-Y. Kuang, Y.-Z. Su, G.-F. Chen, Z. Luo, S.-Y. Xing, N. Li, Z.-Q. Liu, g-C3N4 decorated ZnO nanorod arrays for enhanced photoelectrocatalytic performance, Appl. Surf. Sci. 358 ((2015) 296–303, https://doi.org/10.1016/j.apsusc.2015.08.066.

[98] L. Zhang, M. Jaroniec, Toward designing semiconductor-semiconductor heterojunctions for photocatalytic applications, Appl. Surf. Sci. 430 (2018) 2–17, https://doi.org/10.1016/j.apsusc.2017.07.192.

[99] J. Wang, Y. Yu, L. Zhang, Highly efficient photocatalytic removal of sodium pentachlorophenate with Bi3O4Br under visible light, Appl. Catal. B Environ. 136–137 (2013) 112–121, https://doi.org/10.1016/j.apcatb.2013.02.009.

[100] H.T. Evans, J.A. Konnert, Crystal structure refinement of covellite, Am. Mineral. 61 (1976) 996–1000.

[101] X. Li, Y. Pi, Q. Xia, Z. Li, J. Xiao, TiO2 encapsulated in Salicylaldehyde-NH2-MIL-101 (Cr) for enhanced visible light-driven photodegradation of MB, Appl. Catal. B Environ. 191 (2016) 192–201, https://doi.org/10.1016/j.apcatb.2016.03.034.

[102] L.A. Alfonso-Herrera, A.M. Huerta-Flores, L.M. Torres-Martínez, J.M. Rivera-Villanueva, D.J. Ramírez-Herrera, Hybrid SrZrO3-MOF heterostructure: surface assembly and photocatalytic performance for hydrogen evolution and degradation of indigo carmine dye, J. Mater. Sci. Mater. Electron. 29 (2018) 10395–10410, https://doi.org/10.1007/s10854-018-9096-y.

[103] J. Ding, Z. Yang, C. He, X. Tong, Y. Li, X. Niu, H. Zhang, UiO-66(Zr) coupled with Bi2MoO6 as photocatalyst for visible-light promoted dye degradation, J. Colloid Interface Sci. 497 (2017) 126–133, https://doi.org/10.1016/j.jcis.2017.02.060.

[104] L. Narayanasamy, T. Murugesan, Degradation of Alizarin Yellow R using UV/H2O2 advanced oxidation process, Environ. Prog. Sustain. Energy 33 (2014) 482–489, https://doi.org/10.1002/ep.11816.

[105] R.M. Abdelhameed, D.M. Tobaldi, M. Karmaoui, Engineering highly effective and stable nanocomposite photocatalyst based on NH2-MIL-125 encirclement with Ag3PO4 nanoparticles, J. Photochem. Photobiol. A Chem. 351 (2018) 50–58, https://doi.org/10.1016/j.jphotochem.2017.10.011.

[106] Z. Yang, J. Ding, J. Feng, C. He, Y. Li, X. Tong, X. Niu, H. Zhang, Preparation of BiVO4/ MIL-125(Ti) composite with enhanced visible-light photocatalytic activity for dye degradation, Appl. Organomet. Chem. 32 (2018), e4285, https://doi.org/10.1002/aoc.4285.

[107] J. Huang, H. Song, C. Chen, Y. Yang, N. Xu, X. Ji, C. Li, J.-A. You, Facile synthesis of N-doped TiO2 nanoparticles caged in MIL-100(Fe) for photocatalytic degradation of organic dyes under visible light irradiation, J. Environ. Chem. Eng. 5 (2017) 2579–2585, https://doi.org/10.1016/j.jece.2017.05.012.

[108] H. Ramezanalizadeh, F. Manteghi, Synthesis of a novel MOF/CuWO4 heterostructure for efficient photocatalytic degradation and removal of water pol-lutants, J. Clean. Prod. 172 (2018) 2655–2666, https://doi.org/10.1016/j.jclepro. 2017.11.145.

[109] L. Hu, G. Deng, W. Lu, S. Pang, X. Hu, Deposition of CdS nanoparticles on MIL-53(Fe) metal-organic framework with enhanced photocatalytic degradation of RhB under visible light irradiation, Appl. Surf. Sci. 410 (2017) 401–413, https://doi.org/10.1016/j.apsusc.2017.03.140.

[110] Z. Sha, J. Sun, H.S.O. Chan, S. Jaenicke, J. Wu, Enhanced photocatalytic activity of the AgI/UiO-66(Zr) composite for rhodamine B degradation under visible-light irradi-ation, Chempluschem 80 (2015) 1321–1328, https://doi.org/10.1002/cplu. 201402430.

[111] Z. Sha, J. Sun, H.S. On Chan, S. Jaenicke, J. Wu, Bismuth tungstate incorporated zirconium metal–organic framework composite with enhanced visible-light photo-catalytic performance, RSC Adv. 4 (2014) 64977–64984, https://doi.org/10.1039/ C4RA13000F.

[112] S.-R. Zhu, P.-F. Liu, M.-K. Wu, W.-N. Zhao, G.-C. Li, K. Tao, F.-Y. Yi, L. Han, Enhanced photocatalytic performance of BiOBr/NH2-MIL-125(Ti) composite for dye degra-dation under visible light, Dalton Trans. 45 (2016) 17521–17529, https://doi.org/10.1039/C6DT02912D.

[113] Z. Sha, H.S.O. Chan, J. Wu, Ag2CO3/UiO-66(Zr) composite with enhanced visible-light promoted photocatalytic activity for dye degradation, J. Hazard. Mater. 299 (2015) 132–140, https://doi.org/10.1016/j.jhazmat.2015.06.016.